ANNUAL REVIEWS

Annual Review of Chemical and Biomolecular Engineering

Multiscale Lithium-Battery Modeling from Materials to Cells

Guanchen Li[1,2] and Charles W. Monroe[1,2]

[1]Department of Engineering Science, University of Oxford, Oxford OX1 3PJ, United Kingdom; email: charles.monroe@eng.ox.ac.uk

[2]The Faraday Institution, Harwell Campus, Didcot OX11 0RA, United Kingdom

Annu. Rev. Chem. Biomol. Eng. 2020. 11:277–310

First published as a Review in Advance on March 25, 2020

The *Annual Review of Chemical and Biomolecular Engineering* is online at chembioeng.annualreviews.org

https://doi.org/10.1146/annurev-chembioeng-012120-083016

Copyright © 2020 by Annual Reviews. All rights reserved

ANNUAL REVIEWS CONNECT

www.annualreviews.org

- Download figures
- Navigate cited references
- Keyword search
- Explore related articles
- Share via email or social media

Keywords

transport theory, multiscale modeling, lithium-ion battery

Abstract

New experimental technology and theoretical approaches have advanced battery research across length scales ranging from the molecular to the macroscopic. Direct observations of nanoscale phenomena and atomistic simulations have enhanced the understanding of the fundamental electrochemical processes that occur in battery materials. This vast and ever-growing pool of microscopic data brings with it the challenge of isolating crucial performance-decisive physical parameters, an effort that often requires the consideration of intricate interactions across very different length scales and timescales. Effective physics-based battery modeling emphasizes the cross-scale perspective, with the aim of showing how nanoscale physicochemical phenomena affect device performance. This review surveys the methods researchers have used to bridge the gap between the nanoscale and the macroscale. We highlight the modeling of properties or phenomena that have direct and considerable impact on battery performance metrics, such as open-circuit voltage and charge/discharge overpotentials. Particular emphasis is given to thermodynamically rigorous multiphysics models that incorporate coupling between materials' mechanical and electrochemical states.

1. INTRODUCTION

Future lithium-battery technology targets a specific energy of 235 Wh/kg and energy density of 500 Wh/L at the cell level, with a reduction of pack cost to $125 per kilowatt-hour (1). The development of next-generation systems for vehicles also targets high cycling durability, resistance to burning, good low-temperature performance, and fast charging capability.

Modern instruments allow detailed microscopic, spectroscopic, and tomographic characterization of individual materials within a battery cell, from the nanometer to the millimeter scale. Precise control of active-material properties can be achieved by doping or defect engineering. On a larger scale, mesostructural engineering has been enabled by manufacturing methods like three-dimensional printing (2) or field-assisted sintering (3). For the promise of such developments to be realized, microscopic phenomena must be correlated with macroscopic performance.

A cell's macroscopic behavior results from many processes within materials and across interfaces, including local thermodynamics and reaction kinetics as well as transport of mass, charge, momentum, and heat. Numerous experimental and computational studies report phenomena or mechanisms relevant to battery materials, but only a fraction correlate these with macroscopic observables—that is, factors that contribute distinct signatures in cell-level measurements. Key macroscopic characteristics include a cell's open-circuit voltage (OCV), current/voltage characteristics during charge/discharge, impedance spectrum, overall mechanical state, and extent of degradation.

Computational approaches such as density functional theory (DFT) and molecular dynamics provide quantitative fundamental understanding at the atomic scale. Particle and mesoscale modeling show how micrometer-scale phenomena transform ideal bulk-material properties into the phenomenological properties seen in the laboratory. Continuum cell-level modeling uses both fundamental and phenomenological information to predict macroscopic performance characteristics, such as the state of charge, cycling efficiency, electrode utilization, and power capability. Such models can be upscaled to create streamlined reduced-order models applicable to battery management, testing, and control. Successful multiscale modeling should provide bridges to span this wide range of applications.

This review first outlines the theories most commonly used in continuum models of battery performance. Within this framework, we discuss microscopic phenomena within different components of a cell. Sections 3 and 4 then address the microscopic properties of electrodes and electrolytes. Next, in Section 5, we consider chemomechanical interfacial phenomena, including morphological instability and dendrite propagation; these are relevant to the lithium-plating degradation pathway in lithium-ion batteries, but they also impede the development of the lithium-metal anodes on which many next-generation battery architectures rely. Finally, Section 6 touches on future technology, focusing on all-solid-state lithium batteries.

We highlight key properties as well as material-analysis and design strategies that might enhance performance on the macroscale. Generally, we present simpler models in detail, referencing more sophisticated variations or detailed extensions in the accompanying discussion. We consider only interfacial exchange or bulk transport of mass, charge, and momentum; interfacial charge transfer is modeled with basic electrochemical kinetics, without detailed consideration of solid–electrolyte interphase chemistry and structure. Recently, research on thermal processes relevant to battery safety was reviewed by Feng et al. (4), and the solid–electrolyte interphase literature was reviewed by Wang et al. (5). Although we touch on solid-state lithium batteries below, other novel chemistries such as lithium–sulfur and lithium–air are not addressed; interested readers are referred to the comprehensive reviews by Seh et al. (6), Wild et al. (7), and Aurbach et al. (8).

2. CONTINUUM MODELS

2.1. Multicomponent Transport Phenomena

Contemporary lithium-ion cells comprise two porous electrode materials, whose different chemical states drive lithium intercalation or deintercalation during discharge. The electrodes sandwich an inert porous separator; the pores in all three domains are permeated by a liquid electrolyte that supports ion transport but blocks electron flow. Electrochemical potential differences between the electrodes, which contain variable amounts of intercalated lithium, manifest as a voltage difference that can drive electronic current in an external circuit. Almost all lithium-ion batteries use composite electrodes, wherein active particles are connected by a conductive binder that provides a percolation network for electrons, and an electronically insulating polymer separator. These solid components are porous, permeated by an organic-liquid-solvated electrolyte. As the name implies, all-solid-state batteries use solid electrolytes, which in principle allow lithium metal to replace the porous intercalation anode.

This section focuses on concentrated-solution theory, a transport modeling framework whose principles apply generally across cell components. Most of the development here comes from the foundational work of Newman (summarized, e.g., in 9), with a few minor modifications.

Any phase in a battery comprises n chemically distinct molecular or ionic species. The products of species molarities c_k with velocities $\vec{v}_k$ form molar fluxes $\vec{N}_k = c_k\vec{v}_k$, which, together with the external Cauchy stress tensor $\vec{\vec{\sigma}}$, determine the local dynamical state. Molar masses M_k allow definition of the mass density, $\rho = \sum_k M_k c_k$, and mass-average velocity, $\vec{v}$, where $\rho\vec{v} = \sum_k M_k c_k \vec{v}_k$. Similarly, Faraday's constant F and species equivalent charges z_k lead to the excess charge density, $\rho_e = F\sum z_k c_k$, and current density, $\vec{i} = F\sum_k z_k c_k \vec{v}_k$.

Balance equations express the local electrical state, as well as material and momentum continuity. Excess charge produces the mean field $\vec{E}$ according to Poisson's equation,

$$\vec{\nabla}\cdot\left(\epsilon\vec{E}\right) = \rho_e, \qquad 1.$$

where ϵ is the dielectric permittivity. Material balances for every species can be written as

$$\frac{\partial c_k}{\partial t} = -\vec{\nabla}\cdot\vec{N}_k. \qquad 2.$$

In a domain with constant permittivity, the momentum balance relates system dynamics to the action of stress and the quasi-static Lorentz body force $\rho_e\vec{E}$:

$$\rho\frac{\partial v}{\partial t} = -\rho\vec{v}\cdot\vec{\nabla}\vec{v} - \vec{\nabla}\cdot\vec{\vec{\sigma}} + \rho_e\vec{E}. \qquad 3.$$

In multicomponent materials, excess species fluxes can give rise to another apparent stress, similar to a Reynolds stress (10). This diffusion stress is generally small and is neglected.

Hirschfelder et al. (11) applied irreversible thermodynamics to produce Onsager–Stefan–Maxwell (OSM) diffusion equations, which identify the driving forces that induce relative motion of different species; Newman extended this framework to electrochemical systems (see 9). Goyal & Monroe (10) produced modified driving forces that include deformation strain, which the energy-dissipation functional suggests relate to species velocities as

$$-c_k\left[\vec{\nabla}\mu_k - \frac{M_k}{\rho}\left(\vec{\nabla}p + \vec{\vec{\epsilon}}' : \vec{\nabla}\vec{\vec{\tau}}\right)\right] = \sum_{j\neq k} K_{kj}\left(\vec{v}_k - \vec{v}_j\right), \qquad 4.$$

where K_{kj} is a coefficient quantifying drag between species k and j. Here, p is the external pressure, $\vec{\epsilon}'$ is the deformation-strain tensor, and $\vec{\tau} = \vec{\sigma} - p\vec{I}$ is the deformation stress ($\vec{I}$ is the identity tensor). Summing all n OSM equations recovers the Gibbs–Duhem relation, $\sum c_k \vec{\nabla}\mu_k - \vec{\nabla}p - \vec{\epsilon}' : \vec{\nabla}\vec{\tau} = 0$, so only $n - 1$ flux laws in the form of Equation 4 are independent.

The energetics of each species is characterized by an electrochemical potential μ_k, with contributions from the mixing free energy, mechanical stress, and electric field:

$$\vec{\nabla}\mu_k = \frac{RT}{c_k}\sum_{j\neq n}\chi_{kj}\vec{\nabla}c_j + \overline{V}_k\left(\vec{\nabla}p + \vec{\epsilon}' : \vec{\nabla}\vec{\tau}\right) - Fz_k\vec{E}. \quad 5.$$

In this constitutive law, χ_{kj} are so-called thermodynamic factors; the sum over $\vec{\nabla}c_j$ expresses that any independent species-concentration gradient may affect the chemical-activity gradient of k. Property $\overline{V}_k$ represents the partial molar volume. Extensivity of the total volume implies that $\sum_k c_k\overline{V}_k = 1$, which can be adopted as a volumetric equation of state.

Constraints derived from the Gibbs free energy, including the Gibbs–Duhem equation and various Maxwell relations, reduce the number of independent entries in the thermodynamic matrix χ_{kj}. Constitutive laws expressing how $\overline{V}_k$ depends on stress and composition also satisfy a Gibbs–Duhem relation and constrain the electrochemical potentials through Maxwell relations (10). Equilibrium stress–strain relationships are also thermodynamic, and they vary by material (e.g., for a Hookean solid, $\vec{\epsilon}' \propto \vec{\tau}$; for a viscous liquid, $\vec{\epsilon}' = 0$).

The OSM friction factors K_{kj} quantify irreversible energy dissipation due to mass transport—that is, diffusional resistance to composition gradients or migrational resistance to current flow. The kinetic theory of gases (11) suggests that K_{kj} relates to the corresponding binary diffusivity through

$$K_{kj} = \frac{RT}{c_{\text{ref}}}\frac{c_k c_j}{\mathscr{D}_{kj}}, \quad 6.$$

where $\mathscr{D}_{kj}$ is the Stefan–Maxwell diffusivity of species k in species j. An Onsager reciprocal relation guarantees that $\mathscr{D}_{kj} = \mathscr{D}_{jk}$ (12). Usually, one takes the reference concentration c_{ref} to be the total molarity $c_\Gamma = \sum_k c_k$ in liquids and the molarity of available lattice sites c_{lattice} in solid crystals; Fornasiero et al. (13) have discussed conventions for polymers.

A sequence of linear transformations maps multicomponent OSM equations into the form of Nernst–Planck transport laws (14), which are useful for formulating transport problems that consider simultaneous diffusion, convection, and migration. When combined with microscopic balance equations (Equations 1–3) and an appropriate set of thermodynamic state equations, these make up a transport model that applies generally to liquid or solid electrolytes.

2.2. Single-Ion Conductors and Binary Electrolytes

In materials that contain mobile charge carriers, analysis of Poisson's equation (Equation 1) using the Debye–Hückel theory shows that space charge disperses naturally on a length scale of the Debye length. When applied across length scales much larger than a few nanometers, Poisson's equation can be approximated by local electroneutrality, $\rho_e \approx 0$. By linearly combining the species material balances and applying Faraday's law, one can show that local electroneutrality implies a divergence-free current density, $\vec{\nabla}\cdot\vec{i} = 0$.

For a phase containing a single mobile carrier, such as an ideal ionically conductive solid electrolyte or an electronic conductor, the single independent OSM transport equation implies that

$$\vec{i}_{\text{sol}} = \sigma\vec{E}; \quad 7.$$

that is, charge conduction follows Ohm's law, with the conductivity represented by σ.

Battery materials are usually multispecies conductors. Canonical cell models treat the pore-filling liquid as a simple binary electrolyte—a three-species phase comprising a neutral solvent, $k = 0$ with $z_0 = 0$, in which is dissolved a single salt at molarity c, dissociated fully into one cation, $k = +$, and one anion, $k = -$. The salt satisfies $\nu_+ z_+ + \nu_- z_- = 0$, where ν_k is the ion stoichiometry in a formula unit; the total formula-unit stoichiometry is $\nu = \nu_+ + \nu_-$. Local electroneutrality further simplifies the analysis by relating the two ion concentrations: $\nu c = c_+ + c_-$ and $z_+ c_+ = -z_- c_-$. A salt chemical potential μ_e can be defined through the dissociation equilibrium, as $\mu_e = \nu_+ \mu_+ + \nu_- \mu_-$; generally taken to be independent of the electrical state, μ_e may depend on c and p (10).

For a locally electroneutral and isobaric binary electrolyte, there are two independent OSM equations, which rearrange to produce a modified form of Ohm's law:

$$\frac{\vec{i}}{\kappa} = -\vec{\nabla}\left(\frac{\mu_+}{F z_+}\right) + \frac{1 - t_+^0}{F z_+ \nu_+}\vec{\nabla}\mu_e, \qquad 8.$$

in which κ is the ionic conductivity and t_+^0 is the cation transference number relative to the solvent velocity. It is typical to take $\nabla\mu_+/(Fz_+) = \nabla\Phi$, where Φ is the voltage measured by a reference electrode reversible to cations (9, 15). Inversion of the OSM equations also produces a flux-explicit transport law for cations with respect to the solvent velocity:

$$\vec{N}_+ = -\frac{c_+ \mathscr{D} c_T}{\nu R T c_0}\vec{\nabla}\mu_e + \frac{t_+^0 \vec{i}}{F z_+} + c_+ \vec{v}_0, \qquad 9.$$

where $\mathscr{D}$ is the thermodynamic diffusivity. The three phenomenological coefficients in Equations 8 and 9 relate to the three Stefan–Maxwell diffusivities $\mathscr{D}_{0+}$, $\mathscr{D}_{0-}$, and $\mathscr{D}_{+-}$ as

$$\frac{1}{\kappa} = \frac{-RT}{c_T z_+ z_- F^2}\left(\frac{1}{\mathscr{D}_{+-}} + \frac{c_0 t_-^0}{c_+ \mathscr{D}_{0-}}\right), \quad \mathscr{D} = \frac{\mathscr{D}_{0+}\mathscr{D}_{0-}(z_+ - z_-)}{z_+ \mathscr{D}_{0+} - z_- \mathscr{D}_{0-}}, \quad t_+^0 = \frac{z_+ \mathscr{D}_{0+}}{z_+ \mathscr{D}_{0+} - z_- \mathscr{D}_{0-}}. \qquad 10.$$

The model is closed by a thermodynamic constitutive law, which expresses $\nabla\mu_e$ in terms of composition and pressure gradients. This relationship involves a single thermodynamic factor, χ, and a combined partial molar volume for the salt, $\overline{V}_e = \nu_+ \overline{V}_+ + \nu_- \overline{V}_-$.

2.3. Porous-Electrode Theory

Lithium-ion battery electrodes comprise a porous, electronically conductive solid backbone embedded with active material, permeated with the liquid electrolyte. Equations and properties within continuum models are usually homogenized (volume averaged) to account for this multiphasic nature. The typical approach accounts for pore architecture through two geometric factors, the porosity, ε, and the ratio of pore surface to volume, a.

Doyle, Fuller, and Newman's implementation of porous-electrode theory for lithium-ion batteries (see 16–18) describes electrode domains as a superposition of two phases, in which transport is described by models of the type outlined above. Inside simulation volume elements, balance equations communicate through electrochemical-kinetic source terms, which account for exchange processes between the two phases (9). Also, an additional dimension of the model describes diffusional relaxations of intercalated lithium within active-material particles, as shown in **Figure 1**.

Sulzer et al. (19) developed a nonisobaric porous-electrode model of a lead–acid battery. It allows changes in average liquid composition and concomitant liquid-volume changes during cycling and permits the electrode porosity to contract or dilate. Most lithium-ion battery models

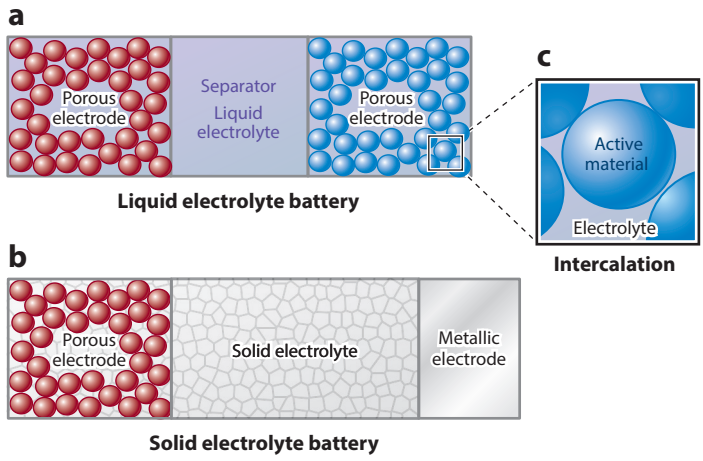

Figure 1

The multiscale battery models discussed in the text assume cell architectures with (*a*) a liquid electrolyte, with a porous anode and cathode, or (*b*) a solid electrolyte, with a metallic anode and a porous cathode. Both cases require (*c*) a local model of transport in active-material particles.

assume that average electrolyte composition and pore geometry remain constant, so we adopt those assumptions here.

Liquid-phase cation flux $\vec{N}_+$ and current density $\vec{i}_{\text{liq}}$, as well as the solid-phase current density $\vec{i}_{\text{sol}}$, are averaged across the entire two-phase volume element within the porous electrode. Cation continuity in the pore-filling liquid is governed by

$$\frac{\partial(\varepsilon c_+)}{\partial t} = a j_{+,n} - \vec{\nabla} \cdot \vec{N}_+, \qquad 11.$$

where $j_{+,n}$ is the net influx of cations normal to the pore walls and c_+ represents the cation concentration in the pore-filling liquid. A law for charge continuity in the pore-filling liquid can be derived by taking into account that anion continuity satisfies a similar law, then applying liquid-phase electroneutrality and Faraday's law:

$$\vec{\nabla} \cdot \vec{i}_{\text{liq}} = a i_n, \quad i_n = F z_+ j_{+,n} + F z_- j_{-,n}. \qquad 12.$$

Charge continuity demands that the total current is solenoidal: $\vec{\nabla} \cdot \vec{i}_{\text{liq}} + \vec{\nabla} \cdot \vec{i}_{\text{sol}} = 0$.

For isobaric electrodes with constant porosity permeated by a binary electrolyte, Equations 9 and 11 combine to show that

$$\varepsilon \frac{\partial c_+}{\partial t} = \vec{\nabla} \cdot \left(\varepsilon D_{\text{eff}} \vec{\nabla} c_+ \right) - \frac{\vec{i}_{\text{liq}} \cdot \vec{\nabla} t_+^0}{z_+ F} + a \left(1 - t_+^0\right) j_{+,n}. \qquad 13.$$

The effective Fickian diffusivity D_{eff} derives from $\mathscr{D}$ but also includes composition-dependent thermodynamic information (15, 20) and dispersive effects due to pore tortuosity (see Section 4). Liquid-phase current follows Equation 8, with κ replaced by an effective conductivity κ_{eff} and $\mu_+/F z_+$ by the liquid-phase voltage Φ_{liq}. Current in the solid phase follows Equation 7, with the conductivity replaced by an effective value σ_{eff} and the solid-phase voltage Φ_{sol} defined through the standard quasi-electrostatic formula $\vec{E} = -\vec{\nabla}\Phi_{\text{sol}}$.

Faradaic current density at the pore surface, i_n, relates to c_+, Φ_{liq}, and Φ_{sol} through electrochemical kinetics. Typically, kinetics is taken to follow the Butler–Volmer equation,

$$i_n(\eta) = i_0 \left[\exp\left(\frac{\alpha_a z_+ F}{RT} \eta \right) - \exp\left(-\frac{\alpha_c z_+ F}{RT} \eta \right) \right], \quad 14.$$

in which i_0 is the exchange-current density and α_a and α_c are anodic and cathodic transfer coefficients, respectively. Generally, i_0 is a function of composition (that is, c_+, and perhaps the surface concentration of intercalated lithium). The surface overpotential η is defined as

$$\eta = \Phi_{liq} - \Phi_{sol} - U, \quad 15.$$

in which U stands for a composition-dependent (and state-of-charge-dependent) OCV relative to the same reference electrode used for Φ_{liq}. Sometimes effects due to film resistance or interfacial capacitance are added to this expression (9). Given a half reaction involving n_{e^-} electrons with lithium-ion stoichiometry s_+, the relation

$$j_{+,n}(\eta) = -\frac{s_+}{n_{e^-} F} i_n(\eta) \quad 16.$$

can be used to replace interfacial source terms with functions of η and composition.

Finally, lithium diffusion within the active materials is considered (17). As well as depending on c_+, OCV is a functional of the intercalated-lithium distribution (cf. Section 3.1). The concentration of intercalated lithium at the active-particle surface, $c_{Li}|_{surf}$, is found through a transport model within the particle under a boundary condition where $j_{+,n}$ determines the surface flux. Typically, intercalated lithium is assumed to be neutral, and intercalation is modeled as a binary diffusion process. Thus, particle interiors evolve as

$$\frac{\partial c_{Li}}{\partial t} = -\vec{\nabla} \cdot \vec{N}_{Li}, \quad 17.$$

and a single OSM equation governs the diffusive flux of intercalated lithium.

3. ELECTRODE ACTIVE MATERIALS

3.1. Equilibrium Energetics

Active materials are generally intercalation compounds or alloys that provide host structures for lithium atoms. Desirable materials afford high energy density, fast lithium transport, and good electrochemical and chemical stability (or metastability). These characteristics are determined by the atomic structures of the materials.

For a given system in which n_{Li} lithium atoms are intercalated, the Gibbs free energy,

$$G = E - TS + pV, \quad 18.$$

in which E is the internal energy, S the entropy, and V the volume, contains all relevant information about equilibrium material properties. Computational methods acquire Gibbs energies systematically from ab initio calculations. Once G is known, the OCV, U, can be measured by differencing the electron electrochemical potentials in the electrodes:

$$U = \frac{\mu_{e^-}^{cathode} - \mu_{e^-}^{anode}}{F z_{e^-}}. \quad 19.$$

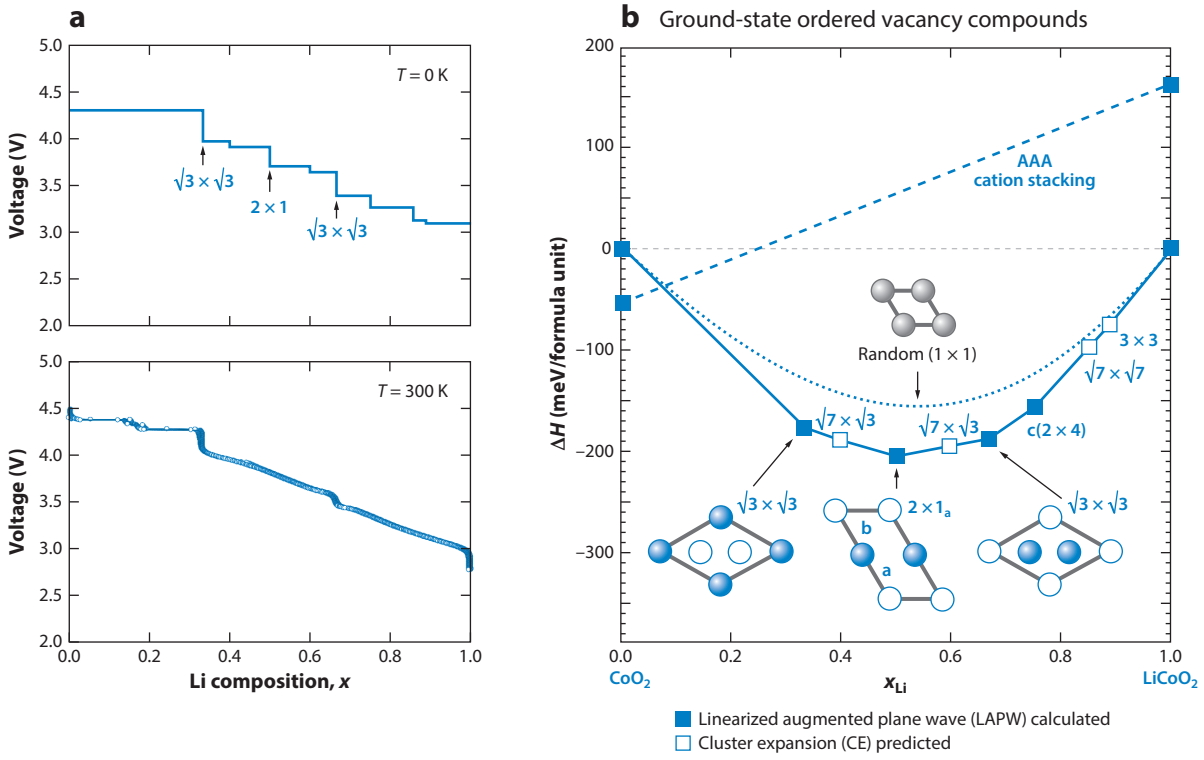

Figure 2

(*a*) Open-circuit voltage of Li_xCoO_2 at $T = 0$ K and $T = 300$ K. Finite temperature smears the sharp discontinuities apparent in the 0 K energetics. (*b*) Predicted ground-state ordered vacancy structures and energetics of Li_xCoO_2. Formation enthalpies ΔH for random (*dotted line*) and ordered AAA-stacking (*dashed line*) arrangements of Li in vacancies are compared with the energy-minimizing structures predicted by density functional theory (*solid line*). Two-dimensional representations of some predicted structures are shown schematically (*filled circles* indicate Li; *empty circles*, vacancies). Figure adapted with permission from Reference 22; copyright 1998 American Physical Society.

In half-reaction equilibrium with a lithium-ion-containing electrolyte, intercalated lithium in an electrode satisfies $\mu_{Li}^{electrode} = \mu_{Li^+}^{electrolyte} + \mu_{e^-}^{electrode}$. Practically, $\mu_{Li}^{electrode}$ is calculated by removing a lithium from the lattice: $\mu_{Li}^{electrode}(T, p, n_{Li}) = G(T, p, n_{Li}) - G(T, p, n_{Li} - 1)$.

Electrostatic energy accounts for most of the chemical potential for isothermal, isobaric intercalation. DFT calculates the minimum electrostatic energy of a stable supercell at zero temperature in vacuum, E_{static} $(T = 0, p = 0)$, generally presented as the formation energy with respect to stable phases, E_f $(Li_xX) = E_{static}$ $(Li_xX) - xE_{static}$ $(Li^0) - E_{static}$ (X), in which Li^0 and X are pure lithium and pure fully delithiated intercalation material, respectively. This formation energy approximates the system's internal energy well when the temperature is not too high. Ignoring entropic and mechanical contributions, the chemical potential of intercalated lithium is $\mu_{Li}(x) = \partial E_f(Li_xX)/\partial x$; since the lithium-oxidation half reaction requires that $\mu_{Li}(x) = FU$, this directly yields the OCV with respect to a metal reference. Thus, an OCV curve for a specific lithium-hosting solid follows from DFT calculations of the minimum energy lattice structures at all stable lithium contents; **Figure 2*a*** shows an example.

The OCV curves of many intercalation compounds exhibit discontinuities, which correspond to phase transitions, as shown by the example in **Figure 2*b***. Phase transitions can occur due to sublattice structure reforming (first order) or through ordering of intercalated atoms (second

order). The early DFT calculations for lithium–tin alloys by Courtney et al. (21) clearly revealed first-order phase transitions and agreed well with experiments. Layered intercalation compounds such as Li_xCoO_2 (22) usually go through second-order order–disorder phase transitions, requiring Monte Carlo simulations (23) to sample the configurational space and identify minimum-energy orderings. For materials with many available intercalation sites, huge numbers of possible intercalation configurations may exist, in which case cluster-expansion techniques can be exploited (24).

At finite temperatures, configurations above the minimum energy will be excited following a Boltzmann distribution, $p_i = e^{-E_i/k_BT}/Z$, where k_B is Boltzmann's constant and $Z = \sum_i e^{-E_i/k_BT}$ is the partition function. Internal energy then becomes an ensemble average of excited states, $\langle E \rangle = \sum p_i E_i$. Energies of excited states are usually approximated by the zero-temperature energies of their configurations, $E_i \simeq E_i$ ($T = 0$, $p = 0$). For materials that allow large numbers of configurations, the configurational entropy $S = -k_B \sum p_i \ln p_i$ will contribute significantly to the Gibbs energy, stabilizing disordered phases. These finite-temperature effects smear discontinuities in OCV curves, as shown in **Figure 2*a***.

DFT also allows electronic conductivity to be analyzed from band structures. Although thermal excitation of electrons minimally affects G, heat can excite electrons from covalent bands into conductive bands, strongly affecting the conductivity's temperature dependence (25). Intercalation can be accompanied by substantial changes in band structure. Ménétrier et al. (26) showed that Li deintercalation from $LiCoO_2$ can cause an insulator–metal transition. Electron entropy can also stabilize phases, as found by Zhou et al. (27) for $LiFePO_4$.

3.2. Transport in the Crystal Lattice

Atomistic computation provides insight into intercalated-lithium transport, which is relatively slow and is consequently crucial to a cell's power capability. Solid diffusion can be regarded as a site-hopping process, whose rate is given by transition state theory as (28)

$$k(T) = \nu^* e^{-\frac{\Delta G^\ddagger}{RT}}, \qquad 20.$$

where ν^* is an attempt frequency of 10^{11}–10^{13} Hz (29) and $\Delta G^\ddagger$ is the activation barrier, defined as the energy difference between the initial state and the transition state. Calculations find the transition state by locating the saddle-point energy on the potential energy surface that contains the initial and final states, as shown in **Figure 3**.

The thermodynamic diffusivity of lithium is taken to be the jumping diffusivity from a random-walk process (30). For a one-dimensional channel in the dilute-carrier limit, $\mathscr{D}(T) = a^2 k(T)$ (31). When interactions between states are more complex, gradients in concentration do not precisely mirror gradients in mobile-species activity, mandating the use of a chemical diffusivity $D = \mathscr{D}\chi_{Li}$.

Activation barriers and thermodynamic factors are both important. Van der Ven & Ceder (32, 33) predicted that Li diffuses through a divacancy mechanism in Li_xCoO_2 for $0 < x < 1$, whose activation barrier depends strongly on x, causing $\mathscr{D}$ to vary across orders of magnitude. In Li_xTiS_2, accounting for lithium–lithium interaction energetics shows that χ_{Li} varies by a factor of 10^4 between the dilute-lithium and dilute-vacancy limits (29). Lithium transport pathways can extend in multiple spatial dimensions, which also affect diffusivity: There is a one-dimensional pathway in $LiFePO_4$ (31), a two-dimensional pathway in $LiCoO_2$ (32), and a three-dimensional pathway in $Li_7La_3Zr_2O_{12}$ (LLZO) (34). Higher-dimensional pathways tend to have larger diffusivities.

Microscopic lithium transport correlates with some macroscopic effects. Malik et al. (35) revealed that one-dimensional diffusion in $LiFePO_4$ makes lithium diffusivity particle size dependent because longer paths are more likely to be blocked by defects. Besides direct hopping, concerted or collective mechanisms have been reported with lower $\Delta G^\ddagger$. He et al. (36) surveyed

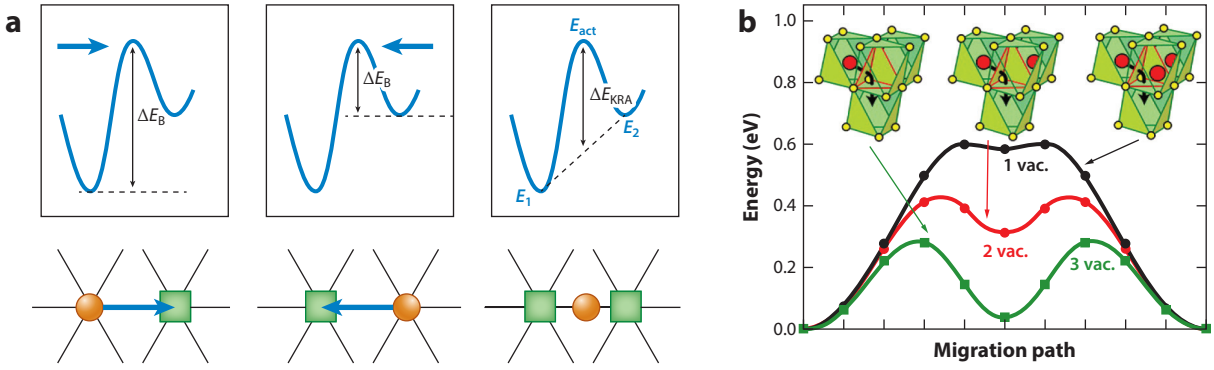

Figure 3

(*a*) Parameters describing a diffusion barrier in a crystal lattice. The energies of the initial state, final state, and intermediate state are denoted by E_1, E_2, and E_{act}, respectively. The migration barrier ΔE_B generally depends on the direction of the hopping process, indicated by an arrow; ΔE_{KRA} illustrates the direction-independent kinetically resolved activation (KRA) barrier defined by Van der Ven et al. (149). Circles and squares denote lithium atoms and vacancies, respectively. Panel *a* adapted with permission from Reference 149; copyright 2001 American Physical Society. (*b*) Migration barriers for hops between neighboring octahedral sites in $LiTiS_2$ spinel. The yellow circles denote sulfur anions coordinating titanium cations, and the red circles denote lithium atoms. Panel *b* adapted with permission from Reference 150; copyright 2013 American Chemical Society.

ion diffusion in a series of fast ion conductors, revealing that mobile ions occupying high-energy sites can activate concerted migration with a reduced diffusion barrier.

More information about computational methods in battery materials research can be found in the recent reviews by Islam & Fisher (37) and Urban et al. (38). Van der Ven et al. (39) provided a clear discussion of computational methods for multicomponent crystalline phases, and Li & Chueh (40) surveyed the computations on intercalation materials.

3.3. Transport in Particles

The solid matrix of a porous electrode comprises active-material particles, a binder, and a conductive filler, but formation of an electron-percolation network requires only a very sparse network of the filler and binder, so the active material is almost entirely surrounded by liquid electrolyte. Most continuum models assume roughly spherical, isotropic solid particles, in which lithium intercalation is a one-dimensional diffusion process; Equation 2 becomes

$$\frac{\partial c_{Li}}{\partial t} + \frac{1}{r^2}\frac{\partial}{\partial r}\left(r^2 N_{Li}\right) = 0. \qquad 21.$$

Reaction kinetics (Equations 14–16) determines fluxes at the particle's surface; fluxes vanish at its center. Intercalated lithium is usually neutral: In the simplest case, we have $N_{Li} = -D_{Li}\partial c_{Li}/\partial r$.

Particle size affects lithium transport profoundly. Darling & Newman (41) studied a porous intercalation electrode with two characteristic particle sizes following various distributions and confirmed that smaller particles are utilized more at larger current densities. Nonuniform particle-size distributions usually affect capacity versus rate behavior negatively, with a more pronounced effect at constant voltage than at constant current.

3.3.1. Chemomechanics. A notable volume change usually accompanies active-material lithiation or delithiation. Lithiation induces volume expansion of about 5% in $LiMn_2O_4$ (42) and 10% in graphite (43). High-energy-density materials such as alloys can expand as much as 310% (44).

At the particle level, varying lithium occupancy between the surface and the core induces strain, leading to cracking or mechanical fatigue (45). At the cell level, active-material expansion can affect pore geometry and particle connectivity. Diffusion-induced stress is a current problem in particle modeling, reviewed recently by Zhao et al. (46).

Research into chemically induced stress began in the 1960s (47), but Christensen & Newman (48) were among the first battery researchers to consider it. They modeled intercalation in a particle with a freely moving boundary. In a spherical particle, gradients of the local state of charge (SOC) induce both radial and tangential stress, as shown in **Figure 4*b***. The maximum stress depends on the charge rate, particle size, and lithium diffusivity. Christensen (49) later incorporated stress diffusion into a porous-electrode cell model, showing pressure diffusion to be less important for conventional intercalation materials and significant when volume expansion is much larger. Zhang et al. (50) studied shape effects: Intraparticle stresses are lower in smaller particles and in ellipsoidal particles with high aspect ratios.

As well as requiring a stress–strain law to model mechanics, deformation can bring about coupled transport through the pressure and strain terms in Equations 4 and 5. In a spherical particle comprising lithium ($k = \mathrm{Li}$) and sites ($k = *$), lattice continuity requires that

$$\frac{\partial c_*}{\partial t} + \frac{1}{r^2}\frac{\partial}{\partial r}\left(r^2 N_*\right) = 0. \qquad 22.$$

The local SOC y is defined as $y = c_{\mathrm{Li}}/c_*$. As an equation of state for volume, one takes the lattice-site concentration c_* to depend on both the local SOC and the Cauchy stress:

$$c_* = c_*^0(y)\, g\left(\vec{\vec{\sigma}}\right) = \frac{1}{y\overline{V}_{\mathrm{Li}}^0 + \overline{V}_*^0} g\left(\vec{\vec{\sigma}}\right), \qquad 23.$$

where $\overline{V}_*^0 = \rho|_{y=0}/M_*$ and $\overline{V}_{\mathrm{Li}}^0 = \rho|_{y=1}/(M_* + M_{\mathrm{Li}})$ are derived by assuming that the material's mass density depends linearly on its lithium concentration (M_* and $\overline{V}_*$ allocate the mass and volume, respectively, of the superstructure surrounding a lattice site to the site itself). Christensen

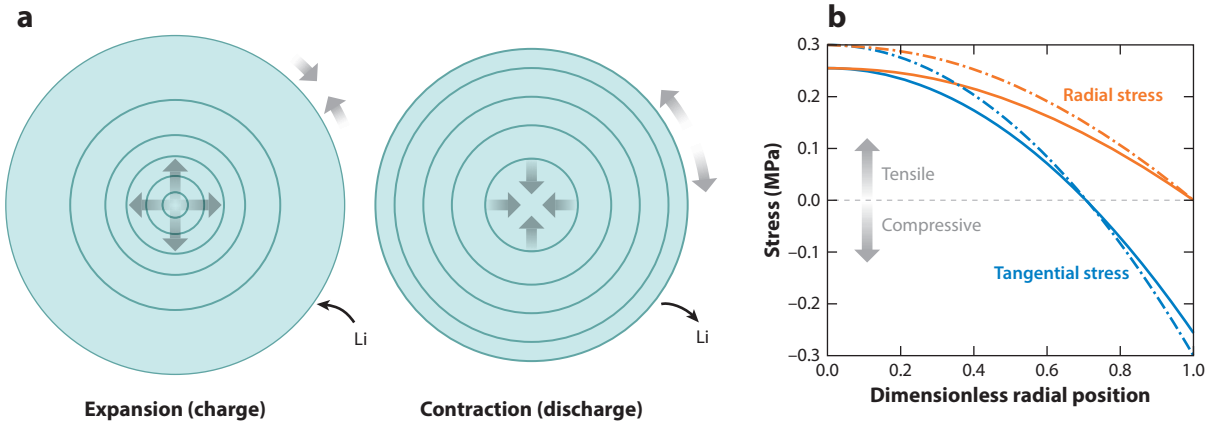

Figure 4

(*a*) Illustrations of stresses in charge and discharge processes. (*b*) The stress distribution in an active-material particle. Dashed lines indicate the case without stress driving diffusion, and solid lines indicate the case with stress driving diffusion. Figure adapted with permission from Reference 48; copyright 2006 Springer Nature.

& Newman (48) proposed that deformation affects concentration through

$$g\left(\vec{\sigma}\right) = \exp\left[-\frac{(1-2\nu_{\mathrm{P}})\left(\sigma_r + 2\sigma_t - 3p^{\theta}\right)}{E_{\mathrm{Y}}}\right], \qquad 24.$$

where σ_r and σ_t are the radial and tangential stresses, p^{θ} is the ambient pressure, ν_{P} is Poisson's ratio, and E_{Y} is Young's modulus. Diffusion follows a single OSM equation,

$$K_{\mathrm{Li}*}\left(\frac{\vec{N}_{\mathrm{Li}}}{c_{\mathrm{Li}}} - \frac{\vec{N}_{*}}{c_{\mathrm{Li}}}\right) = -\chi\vec{\nabla}c_{\mathrm{Li}} - c_{\mathrm{Li}}\left(\overline{V}_{\mathrm{Li}} - \frac{M_{\mathrm{Li}}}{\rho}\right)\left(\vec{\nabla}p + \vec{\epsilon}' : \vec{\nabla}\vec{\tau}\right), \qquad 25.$$

in which $K_{\mathrm{Li}*}$ is the drag the lattice puts on lithium and $\vec{\epsilon}'(\vec{\tau})$ is determined through Hooke's law. The last term on the right describes stress diffusion, which can also be influenced both by the uneven distribution of forces across species and by disparate partial molar volumes. In liquids, stress diffusion is usually negligible, because viscous stresses are small (19). In high-modulus solids, stress diffusion can be significant.

Surface mechanics can affect intraparticle stress as well. Cheng & Verbrugge (51) brought in these phenomena, replacing the free-surface condition with a fixed surface stress,

$$\sigma_r^{\mathrm{surf}} = -\frac{2\sigma_{\theta}^{\mathrm{surf}}}{r_0}, \qquad \sigma_{\theta}^{\mathrm{surf}} = \gamma + K^s\epsilon_{\theta}, \qquad 26.$$

where r_0 is the particle radius, γ is the zero-strain surface tension, and K^s is a surface modulus from the linear-elastic model by Miller & Shenoy (52). Observations universally show that nanoparticles exhibit properties that differ from those of bulk materials, in part because of their enormous surface-to-volume ratios (53, 54). Deshpande et al. (55) rationalized the surprisingly good cycling performance of Si nanowires (56) by showing that intraparticle stress—especially tensile stress—is reduced by surface phenomena.

The mechanical properties of both cathode and anode materials can vary with lithium content (42). Deshpande et al. (57) simulated a cylindrical electrode particle with a concentration-dependent Young's modulus, finding that lithium stiffening can impede surface cracking during delithiation and that lithium softening reduces the tendency to crack at the center during lithiation. Yang et al. (58) studied Cu-coated Si anodes to show that volume change and composition-dependent moduli both affect stress fields.

At the cell level, Steingart and colleagues (59, 60) leveraged the significant changes in mechanical properties during cycling to measure SOC and state of health with acoustic time-of-flight experiments. This method holds promise for almost any closed battery system. Such approaches highlight the significance of macroscopic mechanical effects due to chemical composition changes, and they have great potential for applications in battery management.

3.3.2. Phase separation. As discussed in Section 3.1, many intercalation materials exhibit one or more phase changes during the charging/discharging process. Phase transitions strongly influence the lithium distribution inside particles and also change intercalation dynamics.

Shrinking-core models provide the simplest illustrations of phase change; metal-hydride simulations by Zhang et al. (61) and Subramanian et al. (62) were among the earliest applied to batteries. The latter supposed that a phase with uniform H content appears if surface flux causes lattice saturation, showing that a Fickian diffusion model underestimates the discharge duration for a phase-change cathode with 5-μm particles by more than 10% at a C/4 rate. (A C/x rate means an applied current that will charge or discharge the total rated capacity of the battery in x hours.)

Zhang & White (63) built a shrinking-core model with two phases into a porous-electrode model. They proposed that Li_xCoO_2 supports an α phase at small x and a β phase at large x, both of which can support diffusion. The maximum lithium content of the α phase is $c_{eq,\alpha}$; the minimum in the β phase is $c_{eq,\beta}$. Spherical diffusion spans two spatial domains,

$$\frac{\partial c_\alpha}{\partial t} = \frac{1}{r^2}\frac{\partial}{\partial r}\left(r^2 D_\alpha \frac{\partial c_\alpha}{\partial r}\right), \qquad -D_\alpha \frac{\partial c_\alpha}{\partial r}\bigg|_{r=0} = 0, \qquad c_\alpha|_{r=r_i(t)} = c_{eq,\alpha}, \tag{27.}$$

$$\frac{\partial c_\beta}{\partial t} = \frac{1}{r^2}\frac{\partial}{\partial r}\left(r^2 D_\beta \frac{\partial c_\beta}{\partial r}\right), \qquad -D_\beta \frac{\partial c_\beta}{\partial r}\bigg|_{r=r_0} = \frac{j_n}{F}, \qquad c_\beta|_{r=r_i(t)} = c_{eq,\beta}, \tag{28.}$$

and motion of the interphase boundary is determined by a material balance,

$$D_\alpha \frac{\partial c_\alpha}{\partial r}\bigg|_{r=r_i(t)^-} - D_\beta \frac{\partial c_\beta}{\partial r}\bigg|_{r=r_i(t)^+} = \left(c_{eq,\beta} - c_{eq,\alpha}\right)\frac{\mathrm{d}r_i(t)}{\mathrm{d}t}. \tag{29.}$$

A phase transition within a given particle goes through three stages, shown in **Figure 5*a***: When $r_i(t) = r_0$, the whole particle is in the α phase; when $r_i(t) = 0$, it resides in the β phase; and between these limits, there is a two-phase mixture.

Srinivasan & Newman (64) studied discharge of Li_xFePO_4 by incorporating a two-stage shrinking-core model at the particle level into a porous-electrode model, also considering two particle sizes in the cathode domain. Subsequent experiments revealed an asymmetric response, whose mechanism is sketched in **Figure 5*b***, whereby the particle utilization on charge could be larger than on discharge at transport-limited current densities (65).

Large stresses at phase boundaries are common in phase-transition materials. Christensen & Newman (66) applied a shrinking-core model to $Li_xMn_2O_4$, including stresses due to lithium intercalation along the 4-V plateau and phase change along the 3-V plateau. Fracture at 4 V is likelier at higher currents, whereas the $LiMn_2O_4/Li_2Mn_2O_4$ phase ratio controls fracture at 3 V. Deshpande et al. (67) investigated diffusion-induced stress in phase-transforming electrodes with a moving-boundary model, finding that concentration jumps at phase boundaries lead to stress discontinuities that can cause cracking.

Phase-field models provide another way to simulate phase transitions. These exploit a Cahn–Hilliard chemical potential, with an energy penalty for composition gradients:

$$\mu = \mu_0 + RT \ln \frac{y}{1-y} + RT\chi\,(1-2y) - k\left(\vec{\nabla} y \cdot \vec{\nabla} y\right). \tag{30.}$$

Unlike shrinking-core models, which presuppose a sharp phase boundary at a particular composition threshold, phase-field models produce phase-separation dynamics naturally, at the expense of describing diffusion with a higher-order partial differential equation. As an early application to batteries, Han et al. (68) examined whether diffusion in a phase-separated material would follow Fickian behavior and affect the experimental measurement of diffusivity. They found that the galvanostatic and potentiostatic intermittent titration techniques (69, 70) still yield accurate diffusivities in systems described by phase-field models, even with significant gradient-energy terms. Singh et al. (71) extended the formulation of Han et al. by incorporating surface-reaction kinetics and anisotropic lithium diffusion. The gradient energy affects reaction kinetics by changing the apparent overpotential. In $LiFePO_4$, a typical diffusive shrinking core forms when the dynamics is bulk transport limited, but a new regime of surface-reaction-limited dynamics exists where the phase boundary extends from surface to surface along planes of fast ionic diffusion. Bai et al. (72)

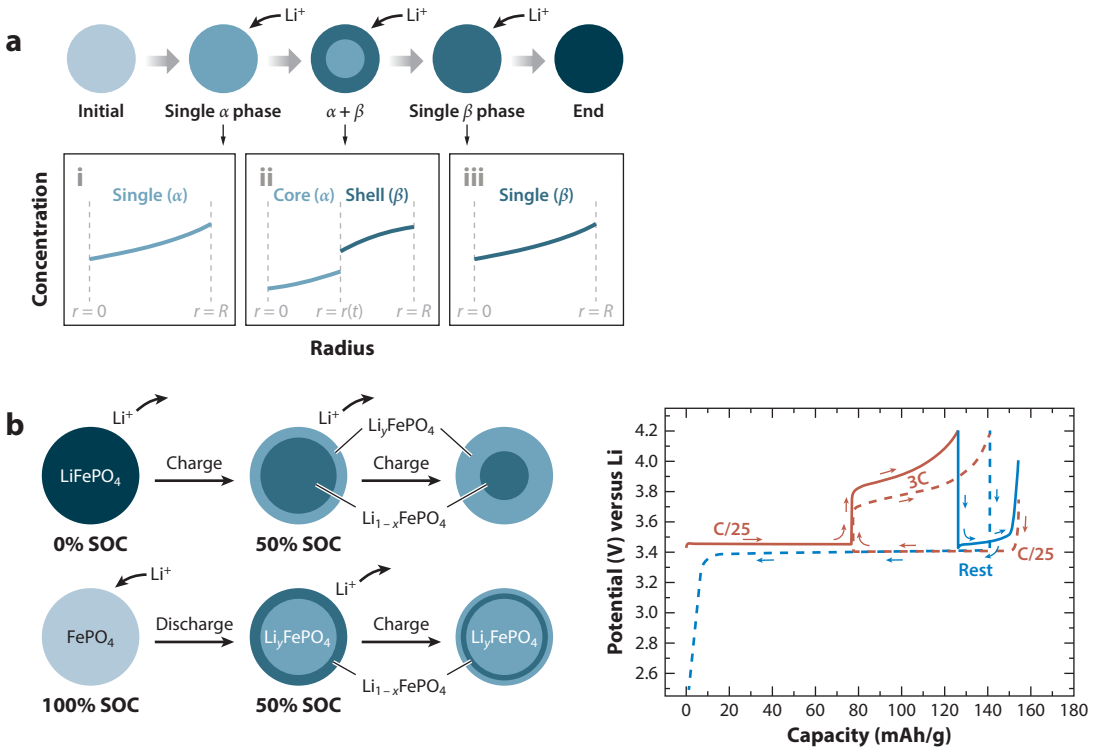

Figure 5

(*a*) The three-stage shrinking-core model of an intercalation particle. Panel *a* adapted with permission from Reference 63; copyright 2007 The Electrochemical Society. (*b*) Path-dependent charging in a particle with phase separation. The electrode is charged from a 0% state of charge (SOC) to 50% at a C/25 rate, after which a 3C charge is performed (*solid red line*). (A rate of C/*x* means that the current will charge or discharge the entire rated capacity in *x* hours.) The electrode is then fully charged at C/25 (*solid blue line*), then discharged to 50% at C/25, after which a 3C charge is performed (*dashed red line*). Finally, the electrode is fully discharged at C/25 (*dashed blue line*). The two 3C charge steps follow different paths. Panel *b* adapted with permission from Reference 65; copyright 2006 The Electrochemical Society.

created a theory of reaction-limited intercalation to show that higher currents can suppress phase separation, explaining an experimentally observed current-induced transition from particle-by-particle to concurrent intercalation (73).

Diffusion-induced stress shapes the dynamics of phase transitions profoundly, especially in nanoparticles. Tang et al. (74) incorporated mechanics into phase-field theory to model amorphization in nanoscale olivines (75). They predicted a critical particle size, below which a low-surface-energy amorphous phase forms to relieve stress. Experiments show that the miscibility gap of nanoscale insertion materials depends on the particle size (76) and SOC (77). Zhang & Kamlah (78) rationalized the size dependence of the miscibility gap in terms of the ratio between the thickness of the interface between phases and the particle size, and they related its average-concentration dependence to the global gradient-energy evolution.

4. LIQUID ELECTROLYTES

4.1. Binary-Electrolyte Models

Nernst–Planck dilute-solution theory provides the simplest dynamical model of a liquid electrolyte, ignoring solute–solute interactions and the finite volume occupied by salt. Newman's

concentrated-solution theory (outlined in 9) applies better to battery electrolytes, which are generally moderately concentrated. At the 1 M concentration typical for lithium-ion battery electrolytes, dissolved salt occupies 5–10% of the liquid volume (20). When current passes through such a solution, the induced salt flux can drive bulk convection. Newman & Chapman (79) clarified this phenomenon by introducing the volume-average velocity $\vec{v}^{\square}$ as a reference for convection. For a binary electrolyte,

$$\vec{v}^{\square} = \overline{V}_{\mathrm{e}} \left[\left(1 - t_+^0\right) \frac{\vec{N}_+}{\nu_+} + t_+^0 \frac{\vec{N}_-}{\nu_-} \right] + \overline{V}_0 \vec{N}_+. \qquad 31.$$

With this and Faraday's law, the cation flux law from Equation 9 for an isobaric system becomes

$$\vec{N}_+ = -D\vec{\nabla}c_+ + \frac{t_+^0 \vec{i}}{Fz_+} + c_+ \vec{v}^{\square}, \qquad 32.$$

where $D = \mathscr{D}\chi c_{\mathrm{T}}/c_0$ is the Fickian diffusivity. Insertion into a cation balance in the form of Equation 2 shows that the evolution of salt concentration follows

$$\frac{\partial c}{\partial t} + \vec{\nabla} \cdot \left(c\vec{v}^{\square}\right) = \vec{\nabla} \cdot \left(D\vec{\nabla}c\right) - \frac{\vec{i} \cdot \vec{\nabla} t_+^0}{z_+ \nu_+ F}, \qquad 33.$$

as expected. Together, the three material balances also imply volume continuity:

$$\vec{\nabla} \cdot \vec{v}^{\square} + \overline{V}_{\mathrm{e}} \frac{\vec{i} \cdot \vec{\nabla} t_+^0}{z_+ \nu_+ F} = -D \frac{\vec{\nabla}c \cdot \vec{\nabla}\overline{V}_{\mathrm{e}}}{1 - c\overline{V}_{\mathrm{e}}}. \qquad 34.$$

In the Doyle–Fuller–Newman lithium-ion battery model (16–18), the volume occupied by salt is explicitly neglected, by an assumption that $\overline{V}_{\mathrm{e}} \approx 0$, in which case $\vec{v}^{\square} \approx \vec{v}_0$ and both vanish uniformly.

Finite salt volume does affect liquid-phase transport, however. The most significant phenomenon is faradaic convection, a bulk flow induced by heterogeneous electrochemistry. For a surface reaction $\sum s_k M_k^{z_k} \rightleftharpoons n_{\mathrm{e}^-} \mathrm{e}^-$, the interfacial volume balance is (80)

$$\left(\vec{v}^{\square} \cdot \vec{n}\right)\big|_{\mathrm{surf}} = \frac{\Delta\overline{V}_{\mathrm{rxn}}^{\mathrm{sol}}}{Fz_{\mathrm{e}^-} n_{\mathrm{e}^-}} \left(\vec{i} \cdot \vec{n}\right)\Big|_{\mathrm{surf}} + \left(\vec{v}_{\mathrm{conv}} \cdot \vec{n}\right)\big|_{\mathrm{surf}}, \qquad 35.$$

where $\vec{v}_{\mathrm{conv}}$ describes interfacial motion due to swelling/contraction or deposition/stripping of solid material, and $\Delta\overline{V}_{\mathrm{rxn}}^{\mathrm{sol}} = \sum \overline{V}_k s_k$ is the liquid-volume change of the reaction. Liu & Monroe (20) identified a dimensionless ratio that measures how convection in Equation 33 compares with diffusion, which equals the salt volume fraction for typical lithium-battery electrolytes. Faradaic convection raises limiting currents and lowers concentration polarization, possibly explaining the high apparent cation transference of ultraconcentrated electrolytes (81, 82).

4.2. Beyond Binary Electrolytes

Practical battery electrolytes contain more than three chemical species. Ion transport is constrained by charge continuity, a limitation that can be alleviated by adding a supporting electrolyte. Yariv & Almog (83) studied Nernst–Planck charge transport in such a system, finding an enhanced concentration of reactive cations near the electrodes. Species–species interactions in concentrated solutions can be important, even when concentrations are relatively low. Monroe (84) showed that interactions between dissolved salt and oxygen in metal–air battery electrolytes can manifest substantial diffusion potentials.

Ion association can produce additional charged or neutral species (such as solvent–ion complexes, ion triplets, or ion pairs), the presence of which has been considered as a possible source of some phenomena observed in concentrated electrolytes. Gebbie et al. (85) and Lee et al. (86) discussed how ion pairing can dilate ionic-liquid double layers. Richardson et al. (87) considered how ion pairing might explain negative transference numbers acquired from inverse modeling of concentration profiles with Nernst–Planck equations.

More complex pairing equilibria can occur in multicomponent electrolytes. Clark et al. (88) developed a framework to account for mobile species in local chemical equilibrium, treating equilibrated groups as quasiparticles that move together. Cell-level performance of pH-buffered aqueous electrolytes in zinc–air batteries was modeled within the framework, showing that slow mass transport limits the effectiveness of the pH buffer.

Solvation is another important factor in electrolytic transport, whose impact on macroscopic transport properties can be assessed with molecular dynamics (89). Li et al. (90) studied transport properties and Li^+ solvation in an solution of lithium bis(trifluoromethanesulfonyl)imide ($LiNtf_2$) salt in an ionic liquid comprising Ntf_2^- anions and *N*-methyl-*N*-propylpyrrolidinium (pyr_{13}^+) cations; all the diffusivities fall sharply as the lithium-salt mole fraction rises. This correlates with an increasing bulk viscosity and the formation of $[Li(Ntf_2)_n]^{(n-1)-}$ solvation structures. Solvation near surfaces is also of interest. Abe et al. (91) pointed out the importance of Li^+ desolvation in interfacial kinetics at the graphite anode. Landstorfer et al. (92) matched specific-capacitance measurements for metal–electrolyte interfaces with a model of adsorption and partial solvation near surfaces. Ultraconcentrated solvent-in-salt solutions may be promising replacements for organic electrolytes (93). McEldrew et al. (94) developed a modified Poisson–Fermi theory for water-in-salt electrolytes that considered electrosorption, solvation, and ion correlations, which reproduced double-layer structures simulated by molecular dynamics. Li^+-solvation-sheath structure also appears to change the formation chemistry of, and the Li^+-migration dynamics within, the solid–electrolyte interphase; the review by Xu (95) provides more details.

4.3. Porous Media

Macroscopic transport in porous media is greatly influenced by pore-network microstructures. The MacMullin number N_M quantifies the effective conductivity of an electrolyte in an insulating porous medium relative to that of the pure electrolyte:

$$N_M = \frac{\kappa}{\kappa_{eff}} = \frac{D}{D_{eff}} = \frac{\tau}{\varepsilon}. \quad 36.$$

Tortuosity τ quantifies how pore structures lengthen diffusion paths. The ensemble-averaged ratio of the shortest path connecting two points in a pore network to the linear distance between them is called geometrical tortuosity, τ^{geo}. A constriction factor β further accounts for cross-sectional area variation along paths: $\tau = \tau^{geo}/\beta$. Geometrical tortuosity has been calculated for simple structures like channel networks (96) or agglomerated spheres (97); recently, three-dimensional X-ray tomography has enabled the calculation of τ^{geo} from real samples (98).

Most often, Equation 36 is used to measure tortuosity phenomenologically, by comparing the effective conductivity measured in an inert porous-solid matrix of known porosity to the conductivity of a pure electrolyte. This knowledge is critical for understanding transport rates in electrolyte-permeated porous separators. Landesfeind et al. (99) recently measured the MacMullin numbers of some commonly used separators with impedance spectroscopy (cf. **Figure 6*a***). Simple models of structured composite materials can provide insight about how microstructures determine MacMullin numbers. Wiener found bounds on the conductivity $\bar{\kappa}$ of an anisotropic

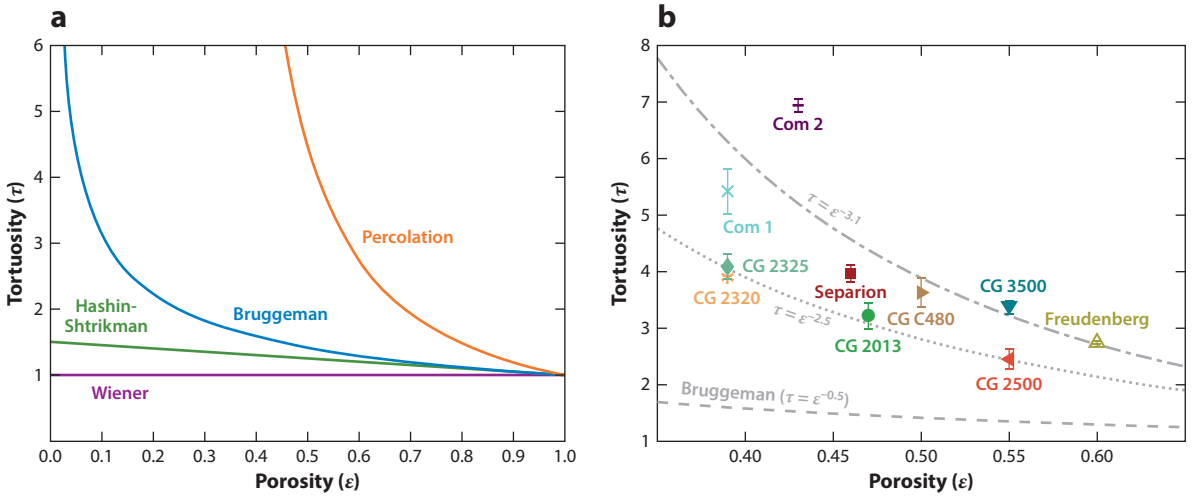

Figure 6

(*a*) A comparison of tortuosity models, showing predictions of percolation theory alongside the standard Bruggeman, Hashin-Shtrikman, and Wiener models. Panel *a* adapted with permission from Reference 104; copyright 2012 The Electrochemical Society. (*b*) The tortuosities of various commercial porous separators and their standard deviations, determined via high-frequency resistance measurements. Labels adjacent to the marks identify various commercial separators produced by Celgard (CG), Freudenberg, and Separion. Two samples from anonymous suppliers are labeled Com 1 and Com 2. Three tortuosity–porosity correlations are shown as gray lines. Panel *b* adapted with permission from Reference 99; copyright 2016 The Electrochemical Society.

binary composite: $(\varepsilon_1/\kappa_1 + \varepsilon_2/\kappa_2)^{-1} \leq \bar{\kappa} \leq \varepsilon_1\kappa_1 + \varepsilon_2\kappa_2$ (see 100), with the limits achieved when the two materials are arranged in series or in parallel, respectively. For isotropic aggregates, the effective conductivities are bounded more tightly, as explained by the Hashin–Shtrikman (HS) model, which assumes random space filling by coated spheres (100). Conductivity is maximized when the coating is more conductive and minimized when it is less conductive. The minimum effective tortuosity of an anisotropic composite is $\tau_{\min}^{\text{Wiener}} = 1$, while that of an isotropic aggregate is $\tau_{\min}^{\text{HS}} = \frac{2}{3-\varepsilon_1}$.

Percolation models apply statistical methods to determine conductivity (101). The simplest suppose a constant-density lattice, within which sites are randomly colored as conductive with a probability equal to the porosity. Conductivity is then calculated from clusters with infinite spanning. Percolation models predict a percolation threshold ε_c, above which these clusters have vanishingly small probability. A simple tortuosity correlation is given by $\tau^{\text{perc}} \simeq \frac{1-\varepsilon_c/\varepsilon}{1-\varepsilon_c}$ for $\varepsilon > \varepsilon_c$. Bruggeman (102) proposed the most widely used tortuosity correlations, $\tau_B = \varepsilon^{-0.5}$ for randomly packed spheres and $\tau_B = \varepsilon^{-1}$ for cylinders, derived by a recursive random embedding process (103). Ferguson & Bazant (104) compared several tortuosity models, as shown in **Figure 6*b***. Laplace's equation has also been solved on real, experimentally determined three-dimensional microstructures (105), and effective transport properties have been extracted from fine-grained simulations (106, 107).

5. INTERFACES

Coupling between diffusion and interfacial reactions appears to be the crucial dynamic that determines battery performance. Interfacial electrochemical reactions are driven by the overpotential, but several physical processes can cause the local overpotential to differ from macroscopically expected values. Since double layers are very thin compared with the lengths across which diffusion

occurs, they are usually ignored in porous-electrode models, although interfacial charging can be accounted for by a capacitive term in Equation 15 (9). Surface passivation can be included as well, by incorporating an ohmic overpotential loss (108).

Lithium plating from a liquid onto metallic lithium causes the formation of mossy or needle-like lithium dendrites, which can ultimately cause short circuits. This dendritic lithium can also form on intercalation-electrode surfaces. If the working current is too high, the reaction speed can exceed the intercalation flux, causing lithium plating. An understanding of interfacial electrodeposition is needed to raise battery power density and cycle life.

5.1. Morphological Stability

One mode of dendrite formation owes to the fact that deposition through a diffusion medium produces naturally unstable surface morphology. During deposition, peaks on a rough surface experience higher salt concentration than do valleys. As a result, deposition on peaks is faster, amplifying roughness. At liquid–metal interfaces, the higher surface-energy cost associated with increased roughness counters this tendency. Mullins & Sekerka (109, 110) developed a pioneering theory to analyze the morphological stability of growing spherical particles and plane solidification fronts in molten binary alloys. Aogaki & Makino (111) and Aogaki (112) applied Mullins–Sekerka analysis to galvanostatic electrodeposition, comparing a three-dimensional, semi-infinite stability analysis to scanning electron micrographs of real interfaces.

Sundström & Bark (113) performed a linear stability analysis of electrodeposition in a parallel-electrode electrochemical cell. Following dilute-solution theory, salt concentration c and potential Φ were found by solving

$$\frac{\partial c}{\partial t} = D\vec{\nabla}^2 c, \qquad \vec{\nabla}\cdot\left[c\vec{\nabla}\left(\frac{Fz_+\Phi}{RT}\right)\right] + P\vec{\nabla}^2 c = 0, \tag{37.}$$

where $D = \frac{\mathscr{D}_{0+}\mathscr{D}_{0-}(z_+ - z_-)}{\mathscr{D}_{0+}z_+ - \mathscr{D}_{0-}z_-}$ and $P = \frac{z_+(\mathscr{D}_{0+} - \mathscr{D}_{0-})}{\mathscr{D}_{0+}z_+ - \mathscr{D}_{0-}z_-}$ arise from the assumptions that $c/\mathscr{D}_{+-} \to 0$, $\chi = 1$, and $c \ll c_0$. Two-dimensional galvanostatic transport was analyzed, assuming that the average current flowed in the y direction and the electrode surface height was a function of position along the x-axis. The surface shape $f(x, t)$ evolves over time as

$$\left(\frac{\partial f}{\partial t} + u\right)\vec{e}_y \cdot \vec{n}_s = -\frac{i_s \overline{V}}{Fz_+}, \tag{38.}$$

where $\overline{V}$ is the molar volume of the metal electrode, $\vec{n}_s$ is a surface-normal vector (in the x–y plane), and $\vec{e}_y$ is a unit vector in the y direction; u is an average convective velocity proportional to the average current, which moves the inertial reference frame to keep the interface at position $y = 0$. The faradaic current i_s is given by Butler–Volmer kinetics, with an overpotential modified to account for the energy cost of surface roughness,

$$\eta_s = \eta + \frac{\overline{V}\gamma}{rF}, \tag{39.}$$

in which $\eta = \Phi - \Phi^{eq}$ is the overpotential that would exist across a smooth interface, γ is the surface energy of the solid–electrolyte interface, and r is the surface's radius of curvature [obtained by analyzing $f(x, t)$]. To assess morphological stability, the surface is subjected to a periodic perturbation, $f(x, t) = f\exp(\alpha t + jkx)$. Then, for a given current and wavenumber k, the eigenvalue α obtained by solving the linearized transport model yields a stable decay ($\alpha < 0$) or unstable growth ($\alpha > 0$) speed for the roughness, shown in **Figure 7*a***. Sundström & Bark found that for any

applied current, there always exists some component of the roughness that will be amplified, so that the liquid–lithium interface is always unstable and the roughening process cannot be prevented by surface forces alone.

Monroe & Newman (114) later incorporated interfacial deformation into electrodeposition kinetics and showed that the stress produced by elastic deformation can stabilize the interface. They extended Equation 39 to include viscous and elastic surface stresses:

$$\eta_s = \eta + \frac{\Delta\mu_{e^-}^{\alpha,\alpha'}}{F}. \qquad 40.$$

The stability parameter $\Delta\mu_{e^-}^{\alpha,\alpha'}$ reflects how the electrochemical potential of electrons in the electrode changes when the electrode–electrolyte interface is transformed from a smooth, unstressed state to a rough, deformed, and stressed state. Through a force balance across the interface, which was taken to be conformal, Monroe & Newman applied thermodynamic principles to show that

$$\Delta\mu_{e^-}^{\alpha,\alpha'} = -\left(\frac{\overline{V}_{Li}^{\alpha'} + \overline{V}_{Li^+}^{\beta'}}{2z_+}\right)\left[2\gamma\mathscr{H} + \vec{e}_n^{\alpha}\cdot\left(\vec{e}_n^{\alpha}\cdot\Delta\vec{\tau}^{\alpha,\beta}\right)\right] + \left(\frac{\overline{V}_{Li}^{\alpha'} - \overline{V}_{Li^+}^{\beta'}}{2z_+}\right)\left(\Delta p^{\alpha,\alpha'} + \Delta p^{\beta,\beta'}\right), \qquad 41.$$

where $\overline{V}_{Li}^{\alpha'}$ and $\overline{V}_{Li^+}^{\beta'}$ are the partial molar volumes of Li in the undeformed electrode (α') and Li^+ in the undeformed electrolyte (β'); $\Delta\vec{\tau}^{\alpha,\beta}$ is the change in the deformation stress across the deformed

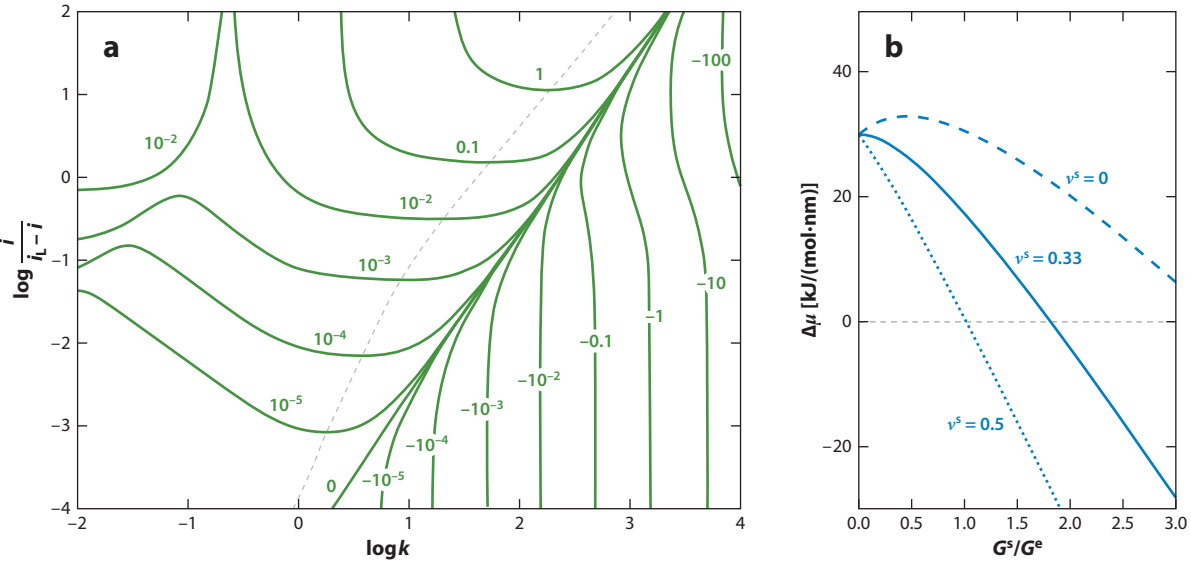

Figure 7

(*a*) The decay or growth speed of the roughness wavenumber k at different currents i; i_L is the limiting current from Equation 43. Panel *a* adapted with permission from Reference 113; copyright 1995 Elsevier. (*b*) The stability parameter $\Delta\mu$ defined after Equation 42 as a function of the shear modulus ratio G^s/G^e between the separator and the electrode. Lines stand for different separator Poisson's ratios ν^s. Panel *b* adapted with permission from Reference 115; copyright 2005 The Electrochemical Society.

interface (α, β); $\Delta p^{\alpha,\alpha'}$ and $\Delta p^{\beta,\beta'}$ are the changes in the gauge pressure on either side of the surface due to interfacial deformation; and $\mathscr{H} = -(1/r_1 + 1/r_2)/2$, where r_1 and r_2 are the principal radii of curvature at the interface. For dilute liquid electrolytes at a two-dimensional interface, the stress and pressure from interfacial deformation vanish, r_2 goes to infinity, and Equation 40 reduces to Equation 39.

Through the use of this overpotential model, the morphological stability of an interface between lithium and a polymer electrolyte (a solid–solid interface) was examined. Monroe & Newman (115) compared the interfacial current density at a flat, undeformed surface with the current in the presence of a sinusoidal deformation with wavenumber k in the small-amplitude limit, showing that

$$\frac{i_{\text{deformed}}}{i_{\text{undeformed}}} = \exp\left[\frac{(1-\alpha_a)\,\Delta\mu_{e^-}^{\alpha,\alpha'}}{RT}\right]. \qquad 42.$$

The parameter $\Delta\mu$ plotted in **Figure 7*b*** divides $\Delta\mu_{e^-}^{\alpha,\alpha'}$ by the shape of the sinusoidal deformation, allowing the stability to be assessed with a single number that is positive when the interface is stable and negative when it is unstable. For a polymer material with a Poisson's ratio similar to that of polyethylene oxide, interfacial roughening is mechanically suppressed when the separator shear modulus is about twice that of lithium (115).

5.2. Dendrite Propagation

Once an electrode surface roughens, the natural concentration and potential gradients induced by cathodic currents encourage the propagation of dendrites toward the opposing electrode. The detailed study of dendrite propagation began with research into zinc electrodeposition (116); theories confirmed for zinc, silver, and copper have been extended to lithium.

Morphological instability acts as an initiation mechanism for dendrites. Other mechanisms are also important, including diffusion-limited aggregation (fractal growth) and space-charge accumulation. Applied current generally polarizes the salt concentration whenever the transference number deviates from 1 (typically $t_+^0 < 0.5$ for lithium electrolytes). Above the limiting current density i_L, given for a planar binary-electrolyte slab by

$$i_L = \frac{2FDc^{eq}}{(1-t_+^0)\,L}, \qquad 43.$$

reactive cations are completely consumed at the cathode surface. At current densities above i_L, the morphology of zinc dendrites is clearly fractal. Diffusion-limited aggregation models have employed random-walk statistics to simulate these fractal shapes and model the growth of deposits (117). Using a route based on dilute-solution transport analysis, Chazalviel (118) analyzed dendrite growth above i_L with a Nernst–Planck model in which local electroneutrality was relaxed by incorporating Poisson's equation. At high currents, a space-charge layer with a vast excess of cations forms near the metal surface, leading to a large overpotential driving dendrite growth, as shown in **Figure 8*c***. Chazalviel also considered the distributions of ions between filaments, finding that wider spacing allows anions to enter the interstices between filaments, encouraging branching. When the spacing of filaments is small, all cations are consumed at their tips; thus, only taller filaments will grow, as shorter ones are starved of ions. In this limit, dendrites are expected to attain bush-like shapes.

The propagation of a needlelike dendrite in a liquid electrolyte has been modeled as a process mitigated by both surface tension and concentration overpotential, which adds the Nernst potential associated with concentration polarization very near the tip to the surface-energy cost

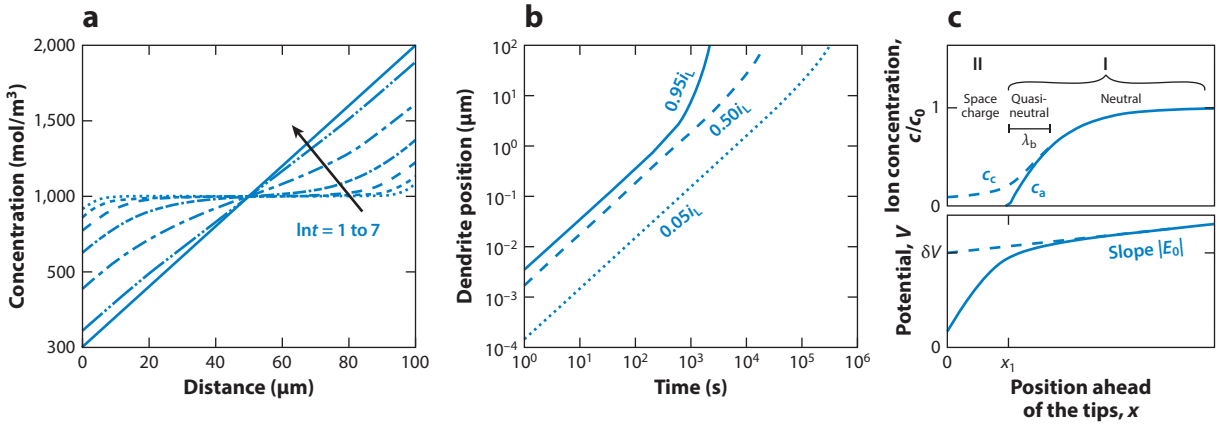

Figure 8

(*a*) Transient development of a salt-concentration profile within a 100-μm-thick binary-electrolyte slab polarized at 99% of the limiting current density (i_L). (*b*) Dendrite growth under different applied currents. Panels *a* and *b* adapted with permission from Reference 122; copyright 2003 The Electrochemical Society. (*c*) Distributions of voltage (V) and the concentrations of cations (c_c) and anions (c_a) near dendrite tips polarized far above the limiting current. The thickness of the space-charge region is x_1; the quasi-neutral region between the space-charge domain and the neutral bulk has thickness λ_b. The ion concentrations and electric field far from the surface are c_0 and E_0, respectively. Panel *c* adapted with permission from Reference 118; copyright 1990 American Physical Society.

associated with the tip's sharpness. Models of this type were first developed by Barton & Bockris (119) and later improved by Diggle et al. (120), who leveraged them to describe dendrite growth in well-supported electrolytes. These models have an advantage over Chazalviel's, in that they rationalize how dendrite growth can occur below the limiting current, as seen when mossy dendrites form in polymer electrolytes (121).

Monroe & Newman (122) extended prior models to unsupported polymer electrolytes. The effect of dendrite tip curvature was incorporated into the dendrite's propagation kinetics. The surface overpotential driving the interfacial reaction at the tip follows

$$\eta_s = \eta + \frac{\gamma \overline{V}_{\mathrm{Li}}}{rF} + \frac{RT}{F} \ln\left(\frac{c^{\delta}_{\mathrm{Li}^+}}{c^{\delta'}_{\mathrm{Li}^+}}\right); \qquad 44.$$

mass transport to the tip causes lithium's surface concentration $c^{\delta'}_{\mathrm{Li}^+}$ to differ significantly from the nearby bulk concentration $c^{\delta}_{\mathrm{Li}^+}$. Assuming pseudosteady spherical diffusion, one obtains

$$i_{\mathrm{n}} = \frac{DF\left(c^{\delta}_{\mathrm{Li}^+} - c^{\delta'}_{\mathrm{Li}^+}\right)}{\left(1 - t^0_+\right) r} \qquad 45.$$

for a hemispherical dendrite tip of radius r. A Butler–Volmer equation at the dendrite tip then shows how the current density varies with the surface energy, tip radius, and overpotential:

$$\frac{i_{\mathrm{n}}}{i_{0,\mathrm{ref}}} = \frac{\exp\left(\frac{2\gamma \overline{V}_{\mathrm{Li}}}{rRT}\right)\exp\left(\frac{\alpha_a z_+ F}{RT}\eta\right) - \exp\left(-\frac{\alpha_c z_+ F}{RT}\eta\right)}{\left(\frac{c_{\mathrm{ref}}}{c^{\delta'}_{\mathrm{Li}^+}}\right)^{\alpha_a} + \frac{\left(1-t^0_+\right) r i_{0,\mathrm{ref}}}{FDc^{\delta'}_{\mathrm{Li}^+}} \exp\left(-\frac{\alpha_c z_+ F}{RT}\eta\right)}. \qquad 46.$$

By assuming a worst-case scenario in which the tip radius maximizes the growth rate, one can solve for how the dendrite propagates by coupling the transient salt concentration profile yielded by a diffusion model, shown in **Figure 8*a***, with the interfacial kinetics, yielding the growth profiles

shown in **Figure 8*b***. Simulations show that cell short circuit would be expected during typical charges above 75% of i_L. The interelectrode distance can be increased to slow cell failure, but the advantages decrease as distance increases. Surface forces have little effect on cell failure—a factor of 1,000 increase in γ delays cell failure by only 6%.

6. ALL-SOLID-STATE BATTERIES

All-solid-state lithium batteries, which employ solid electrolytes, have recently become a popular research topic. By solid electrolytes, we specifically mean inorganic ceramic or ceramic-glass lithium-ion conductors, rather than polymers. Solid electrolytes are generally nontoxic and nonflammable. They tend to have high elastic moduli and good toughness, supporting more stable interfaces that suppress surface roughening during cycling. These favorable properties could enable lithium-metal anodes, supporting a potential doubling of energy density on the cell level.

Most solid electrolytes act as single-ion conductors, meaning that lithium ions carry almost all of the current. This feature eliminates the diffusion polarization that fosters dendrite growth in liquid electrolytes (123) and theoretically suggests that mass transfer should never limit operating power. Oxide garnets (e.g., LLZO) and sulfides (e.g., argyrodite) are promising candidate electrolytes due to their impressive room-temperature ionic conductivities. Atomistic simulations have been widely employed to seek such materials, not only with high conductivity but also with wide stable voltage windows (124). Zhang et al. (125) reviewed contemporary work on solid-electrolyte materials.

Kornyshev & Vorotyntsev (126) were among the first to develop an equilibrium theory for solid single-ion conductors, putting forward a model based on Fermi-distributed charge carriers. Yamamoto et al. (127) probed electric fields near electrode–garnet boundaries, suggesting that space charge penetrates relatively far into the ceramic. Braun et al. (128) attributed these extended space-charge domains to site saturation by mobile cations.

We recently proposed a chemomechanical model of single-ion conductors to study current-induced stresses (129). A single-ion conductor comprises two species: mobile cations (concentration c_+) and stationary, countercharged sites in the sublattice (c_-). The site concentration puts an upper bound on the maximum local cation concentration and is roughly constant ($c_- = c_-^0$) for sublattices with a high bulk modulus that accommodate cations without swelling. In such a lattice, Ohm's law takes the form

$$\frac{\vec{i}}{\kappa} = \vec{E} - \frac{RT}{Fz_+}\vec{\nabla}\ln\left(\frac{c_+}{c_-^0 - c_+}\right) + \frac{M_+}{Fz_+\rho}\vec{\nabla}p, \qquad 47.$$

where the strain energy due to deformation has been neglected. In the presence of a field $\vec{E}$, space charge experiences a force balanced by mechanical pressure, so that $\vec{\nabla}\cdot\vec{\sigma} = \rho_e\vec{E}$ establishes the local momentum balance.

In the bulk of a solid single-ion conductor, local electroneutrality imposes a uniform cation distribution, so transport occurs in a one-in-one-out manner, reducing Ohm's law to $\vec{i} = \kappa\vec{E}$ (cf. Equation 7); profiles of the concentration, electric field, and pressure are uniform in the bulk, as seen in **Figure 9**. Within double layers at the electrolyte's edges, more complex coupling exists between diffusion, migration, and pressure diffusion, as shown by Equation 47. Whether a solid electrolyte acts more like a double-layer capacitor or a bulk resistor is determined by the character of its interfaces—that is, by its interfacial resistance R_{int} and capacitance C_{int}.

Impedance measurements suggest that solid electrolytes behave more like capacitors from an electrical standpoint because their interfacial capacitances are very high (129). Equations 1 and

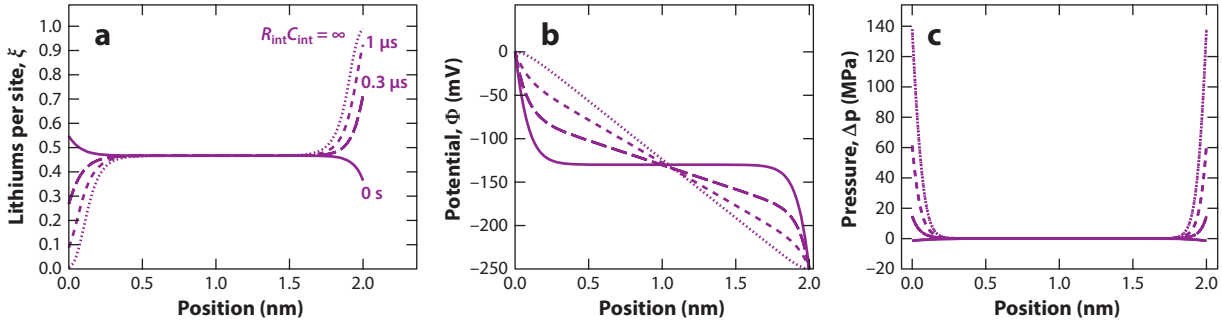

Figure 9

Profiles of (*a*) lithium-ion occupancy, (*b*) electric potential, and (*c*) pressure in an artificially thin film with the properties of $Li_7La_3Zr_2O_{12}$ (LLZO), assuming different interfacial properties: $R_{int}C_{int} = 0$ s, 0.3 μs, 1 μs, and ∞. Figure adapted with permission from Reference 129; copyright 2019 PCCP Owner Societies.

3 show that space charge produces a surface pressure (Maxwell stress) relative to the bulk. Since interfacial roughness has a much larger length scale than the Debye length, this can be computed with a one-dimensional analysis (129), yielding

$$\sigma_{surf} - \sigma_{bulk} \approx \frac{\epsilon}{2}\left(E_{surf}^2 - E_{bulk}^2\right), \qquad 48.$$

where

$$E_{bulk} = \frac{i}{\kappa}, \quad E_{surf} = R_{int}C_{int}i. \qquad 49.$$

This surface stress affects the overpotential across the space-charge layer at the interface, similar to Chazalviel's (118) approach to dendrite growth.

Solid electrolytes indeed inhibit morphological instability and have achieved very good cycling performance at low currents. These materials still suffer from dendrite formation when operated above a critical current, however. The mechanism of this dendrite-formation process does not arise from morphological instability and is not considered within the Monroe–Newman model. Extensive relevant research was done decades ago to understand dendrite formation and critical currents in sodium β alumina. De Jonghe and coworkers (130) defined two degradation modes by experimental observation. Mode I is a rapid penetration of the electrolyte by a sodium-filled crack, while mode II is a slow bulk deposition of sodium, attributed to electronic conductivity of the solid (131). Dendrites in lithium electrolytes tend to fall in the mode I category. Feldman & De Jonghe (132) built a mechanical model to describe how preexisting sodium filaments propagate. An elliptic-cylindrical crack, shown in **Figure 10*a***, is taken to be filled with metal. The average surface current density is found with Laplace's equation and is related to the metal's average velocity $\bar{v}$ through

$$\bar{j} = j_\infty\,(l/r + 1) = z_{M^+}c_M\bar{v}, \qquad 50.$$

where c_M is the metal concentration and z_{M^+} is the ion charge. The metal is lighter and softer than the solid electrolyte and will flow out of the electrolyte crack to the metal side as deposition proceeds. A Poiseuille viscous flow with viscosity τ is assumed, so that

$$\frac{dP}{dx} = \frac{-3\tau\bar{v}}{r^2\,(1 - x^2/l^2)}, \qquad 51.$$

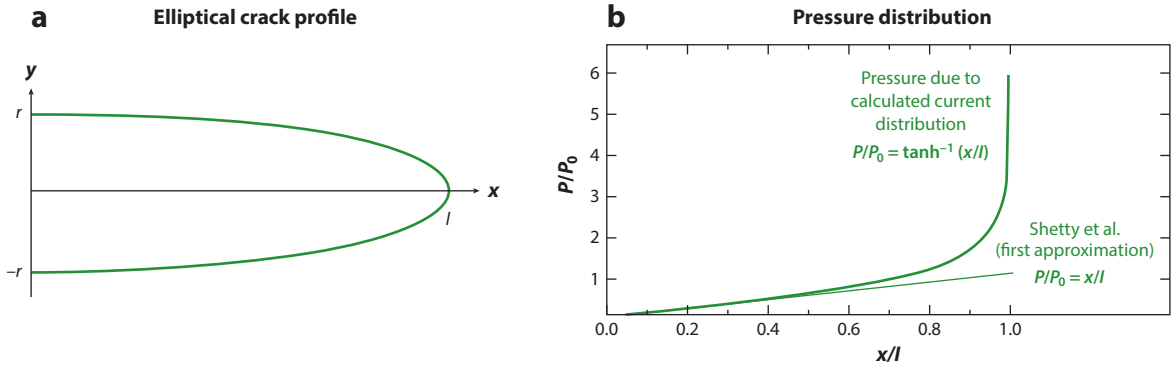

Figure 10

(*a*) An illustration of an elliptic-cylindrical filament of radius r and length l. (*b*) The stress distribution in an elliptic-cylindrical filament; P_0 is the prefactor of the pressure distribution defined in Equation 52. The model from Shetty at al. (151) is a first-order approximation of Feldman & De Jonghe's model (132). Figure adapted with permission from Reference 132; copyright 1982 Springer Nature.

which integrates to

$$P(x) = -\frac{3\tau\bar{v}l}{r^2}\tanh^{-1}\left(\frac{x}{l}\right) = P_0\tanh^{-1}\left(\frac{x}{l}\right). \quad 52.$$

The flow produces a back pressure at the dendrite tip. Nonuniformity of the current distribution causes the tip pressure to be significantly greater than the ambient pressure, as shown in **Figure 10*b***. Dendrite propagation is expected when the tip pressure is greater than the fracture stress of the solid. Critical-current measurements analyzed using this model suggest that the fracture toughness associated with dendrite penetration is about two orders smaller than the toughness determined by mechanical testing, implying that mechanical back pressure is probably not enough to crack the solid electrolyte.

Recently, Porz et al. (133) derived a dendrite-propagation model similar to De Jonghe's (131), assuming that the current focuses on the tip of the dendrite. They related the tip stress to the tip overpotential $\sigma_{\text{tip}} = -F\eta/\overline{V}_{\text{Li}}$ and showed that an overpotential of 16 mV is already enough for a 1-μm-long, 0.2-μm-wide dendrite to grow in polycrystalline Li_2S-P_2S_5 (LPS). According to this analysis, a short circuit should occur if a narrow filament is formed. Thus, unlike for liquid electrolytes, roughening instability at the interface does not initiate dendrite formation. Rather, an initial needlelike structure must exist first. Engineering efforts should therefore target the prevention of filament formation at interfaces between lithium and solid electrolytes.

At a pristine interface, both the high shear modulus and unit transference of the electrolyte successfully improve the interfacial morphological stability at low currents, supporting the very stable cycling performance observed below the critical current. The reason for interfacial failure at high currents is not clear. Ahmad & Viswanathan (134) pointed out the importance of the partial molar volume in Equation 41, of the Monroe–Newman model, which can destabilize interfaces. Kasemchainan et al. (135) discovered different critical currents for the stripping and plating processes in a symmetric cell using lithium electrodes and an argyrodite electrolyte. The stripping critical current is lower than the plating one, because stripping at large currents creates cavities in the metal at the interfaces (lithium pitting), which raises the effective current density at points of metal–electrolyte contact during subsequent plating events.

The application of external pressure effectively suppresses cavity formation and increases the stripping critical current. Krauskopf et al. (136) proposed that vacancies effused from within the

lithium metal accumulate at the interface to create cavities. Wang et al. (137) observed that significant voltage polarization occurs at a current-dependent critical stack pressure and associated this pressure with lithium metal's creep rate, which allows it to flow and fill in voids. The mechanical and transport properties of lithium metal are still not firmly known, especially on the microscale. This limits the development of phenomenological theory. A very detailed report of lithium's mechanical properties was just put forward by Masias et al. (138). Despite the remaining questions about lithium mechanics, metal deformation and flow during the stripping process significantly affect interfacial stability and likely control the critical stripping current.

It should not be ignored that dendrites can form during a single charge step, and the mechanism behind the critical plating current is still uncertain. Once the stripping critical current is mitigated, plating critical currents will become the key factor that limits power performance of all-solid-state lithium-battery electrolytes.

Various experimental routes have been attempted to achieve high critical currents; most hinge on the careful treatment and polishing of interfaces. For the tougher garnet material LLZO, lithium roughening is not observed after long cycling, implying that morphological instability is indeed suppressed and is not responsible for dendrite nucleation. Sharafi et al. (139) measured the critical current at different temperatures and identified interfacial resistance as a key factor that determines critical currents. In a later paper, Sharafi et al. (140) related the interfacial resistance to the adhesive energy, which can be measured via wettability experiments. Removing the Li_2CO_3 surface layer that air exposure forms on LLZO improves its lithium wettability and reduces the interfacial resistance. Fu et al. (141) added an ultrathin layer of a lithium alloy at the interface between lithium and the solid electrolyte, showing that it improved lithium wetting and reduced the interfacial resistance significantly.

As shown in **Figure 11*a***, Cheng et al. (142) observed that dendrites form along grain boundaries in LLZO, which highlights how solid electrolyte microstructure affects failure mechanisms. Voids and grain boundaries offer space for lithium plating and possible paths for dendrite propagation. Polycrystalline LLZO samples prepared by different synthetic routes can have vastly different distributions of grain shape and grain-boundary misorientation angle, inducing different grain-size dependences for critical currents (143, 144). Yu & Siegel (145) simulated grain boundaries in LLZO with molecular dynamics, reporting that the grain-boundary energy and diffusion-activation energy vary for different misorientation angles. Ma et al. (146) revealed severe structural and chemical deviations across a domain about two to three unit cells thick at the grain boundaries of garnet, which could be responsible for slow ion transport at grain boundaries. Recently, Han et al. (123) observed bulk plating of lithium in solid electrolytes and linked smaller electronic conductivity to higher critical currents. It is noteworthy that this hypothesized electron-induced bulk plating is consistent with the mode II mechanism De Jonghe et al. (130) suggested for sodium β alumina.

We proposed a grain-coating mechanism that could rationalize the energetics of dendrite nucleation in mode II, which is schematized in **Figure 11*b***(129). Using Equation 48, we calculated the interfacial stresses corresponding to experimentally determined critical currents. Unlike in mode I dendrite propagation, this interfacial stress is not large enough to open a crack; rather, it raises the overpotential required to plate lithium at the metal surface, as shown in **Figure 11*b***. A comparison between the lithium plating overpotential in a bulk grain boundary, $\eta_{\mathrm{GB,\,bulk}}$, and at the lithium–electrolyte interface, η_{surf}, yields

$$\eta_{\mathrm{surf}} - \eta_{\mathrm{GB,bulk}} = \frac{\overline{V}_{\mathrm{Li}}}{F z_{\mathrm{Li}^+}} \left[p_{\mathrm{surf}} - p_{\mathrm{bulk}} + a_V \left(\gamma_{\mathrm{GB}} - 2\gamma_{\mathrm{surf}} \right) \right], \qquad 53.$$

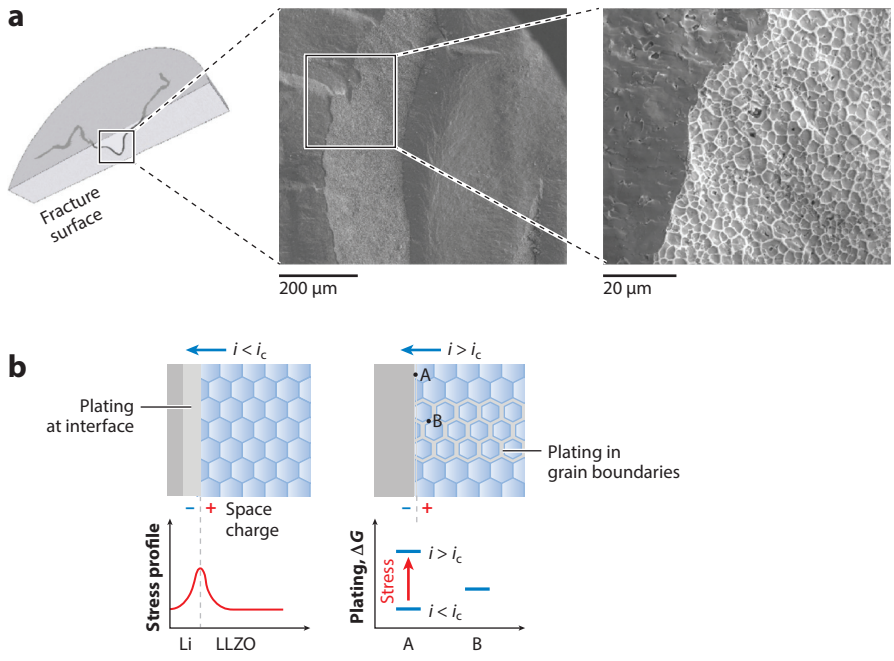

Figure 11

(*a*) The microstructure of a metallic filament in $Li_7La_3Zr_2O_{12}$ (LLZO). Panel *a* adapted with permission from Reference 142; copyright 2017 Elsevier. (*b*) A diagram illustrating the grain-coating mechanism of dendrite formation. Applied current densities (*i*) greater than the critical current density (i_c) induce stress that causes the Gibbs free energy cost for lithium plating (ΔG) to be higher at the interface (location A) than in grain boundaries (location B). Panel *b* adapted with permission from Reference 129; copyright 2019 PCCP Owner Societies.

where γ_{surf} and γ_{GB}, respectively, represent the surface energies of the lithium–electrolyte interface and the grain boundary, and a_V quantifies the surface-to-volume ratio of the grains; lithium plating at the grain boundary is assumed to replace the interface between grains with two new interfaces between solid electrolyte and lithium. Above the critical current, the pressure at the interface induced by space charging makes bulk plating in grain boundaries have lower overpotential; when electrons are available in the bulk, electrochemical coating of lithium around the grain boundaries will occur, providing the initial trigger for mechanical failure.

For porous-electrode composites made up of intercalation compounds and solid electrolytes, the volume change of intercalation particles can produce severe problems, such as fracture or interfacial delamination, because solid electrolytes are generally stiff and some are brittle. Bucci et al. (147) modeled the mechanical degradation of all-solid-state electrodes caused by intercalation-induced expansion of active particles. They suggested that the combination of a low particle-volume expansion and a tough solid electrolyte could prevent interfacial fracture. Counterintuitively, compliant solid electrolytes appear to be more susceptible to microcracking; harder oxides may therefore be more suitable than sulfides for use in composite electrodes, despite sulfides' higher conductivity. Bucci et al. (148) later developed a one-dimensional particle model based on the cohesive theory of fracture to investigate the mechanical stability of the interface between intercalation particles and solid electrolytes. In most cases, delamination occurs if active particles undergo a volume change of about 7.5%. Very compliant electrolytes with large interfacial fracture energy can afford up to a 25% volume change. Interfacial fracture reduces the

contact area with the electrolyte, which slows lithium transport, increases apparent kinetic losses, and affects the charge/discharge rate capability significantly. Materials with a lower yield stress (less than half of the interfacial cohesive strength) may be able to release deformation-induced stress by deforming plastically before delamination happens.

7. CONCLUSION AND OUTLOOK

Multiscale modeling aims at showing how microscopic phenomena can be modified to achieve improvements in macroscopic battery performance. Modern experimental and computational techniques provide a very comprehensive view of individual physical processes that occur at many length scales, and engineering tools exist to understand and predict how these processes interact when materials are assembled into a device. Thermodynamics is the central physical tool that helps to elucidate battery performance and degradation in a complete and consistent way. In equilibrium, the open-circuit potential of a battery is determined by the Gibbs free energy of electrode materials, which may go through various phase changes relating to lattice structure and/or microscopic ordering. Away from equilibrium, thermodynamic principles can be exploited to underpin transport models. Lithium diffusion inside intercalation materials is a bottleneck that places a limit on operating currents. At the particle level, the chemomechanics of active-material particles, especially diffusion-induced stress, plays a central role in electrode degradation.

Practical batteries incorporate concentrated liquid electrolytes, and there is even a hypothesis that solvent-in-salt systems might be beneficial at high powers. The independent transport properties and microscopic structures of highly concentrated liquid electrolytes are generally not well characterized. More theoretical and experimental efforts are needed to understand physical phenomena such as solute-volume effects, which can become relevant at higher concentrations. The microstructures of porous media can greatly influence ion transport in the electrolyte-filled pores. Three-dimensional imaging technology allows a more detailed characterization of porous media, but more effort is needed to provide better universal empirical descriptions of tortuosity to support continuum modeling and device engineering. Diffusion polarization in liquid electrolytes is a dominant factor that drives degradation, for instance, by dendrite formation. The reduction of diffusion polarization by using high-transference electrolytes may impede dendrite growth. Dendrite formation is inevitable at the interface between lithium metal and liquid electrolytes, but morphological instability can be inhibited by introducing stiff and stable interfacial coatings. It is possible to inhibit morphological instability entirely through the use of solid ceramic electrolytes, several of which have suitably high elastic moduli.

Much recent work has shown the promise of all-solid-state lithium batteries. Since diffusion polarization is eliminated in solid ceramic electrolytes, and because they have very high elastic moduli, the interfacial stress that arises in the presence of a voltage bias becomes a crucial factor that determines whether dendrites grow. The lithium diffusivity (conductivity) of solid electrolytes is less important with regard to degradation, whereas the interfacial properties (particularly, surface capacitance and interfacial resistance) and bulk dielectric properties are more relevant. Both crack propagation and bulk plating are important modes of dendrite growth in solid electrolytes. Since dendrite propagation is generally hard to suppress, preventing dendrite nucleation would be more effective. The achievement and retention of good contact between the electrolyte and active-electrode materials are critically important to the design of all-solid-state batteries. Within lithium electrodes, slow lithium flow, which leads to pitting, becomes a limiting performance factor. In composite electrodes, contact loss due to the mechanical fracture between active-material particles and electrolytes will cause performance degradation. A better understanding of chemomechanics would facilitate great improvements in all-solid-state battery development.

DISCLOSURE STATEMENT

The authors are not aware of any affiliations, memberships, funding, or financial holdings that might be perceived as affecting the objectivity of this review.

ACKNOWLEDGMENTS

This work was supported by The Faraday Institution, subawards FIRG003 and FIRG007 under grant EP/S003053/1; the UK Engineering and Physical Sciences Research Council, under grant EP/P003532/1; and the UK Industrial Strategy Challenge Fund: Materials Research Hub for Energy Conversion, Capture, and Storage (M-RHEX), under grant EP/R023581/1.

LITERATURE CITED

1. US Dep. Energy. 2017. *Vehicle Technologies Office annual merit review 2017*. Rep., US Dep. Energy, Washington, DC. **https://www.energy.gov/sites/prod/files/2017/11/f39/2017-vehicle-technologies-office-annual-merit-review.pdf**
2. Zekoll S, Marriner-Edwards C, Hekselman AKO, Kasemchainan J, Kuss C, et al. 2018. Hybrid electrolytes with 3D bicontinuous ordered ceramic and polymer microchannels for all-solid-state batteries. *Energy Environ. Sci.* 11:185–201
3. Becker MZ, Shomrat N, Tsur Y. 2018. Recent advances in mechanism research and methods for electric-field-assisted sintering of ceramics. *Adv. Mater.* 30:1706369
4. Feng X, Ouyang M, Liu X, Lu L, Xia Y, He X. 2018. Thermal runaway mechanism of lithium ion battery for electric vehicles: a review. *Energy Storage Mater.* 10:246–67
5. Wang A, Kadam S, Li H, Shi S, Qi Y. 2018. Review on modeling of the anode solid electrolyte interphase (SEI) for lithium-ion batteries. *NPJ Comput. Mater.* 4:15
6. Seh ZW, Sun Y, Zhang Q, Cui Y. 2016. Designing high-energy lithium–sulfur batteries. *Chem. Soc. Rev.* 45:5605–34
7. Wild M, O'Neill L, Zhang T, Purkayastha R, Minton G, et al. 2015. Lithium sulfur batteries, a mechanistic review. *Energy Environ. Sci.* 8:3477–94
8. Aurbach D, McCloskey BD, Nazar LF, Bruce PG. 2016. Advances in understanding mechanisms underpinning lithium-air batteries. *Nat. Energy* 1:16128
9. Newman J, Thomas-Alyea KE. 2004. *Electrochemical Systems*. New York: Wiley. 3rd ed.
10. Goyal P, Monroe CW. 2017. New foundations of Newman's theory for solid electrolytes: thermodynamics and transient balances. *J. Electrochem. Soc.* 164:E3647–60
11. Hirschfelder JO, Bird RB, Curtiss CF. 1964. *Molecular Theory of Gases and Liquids*. New York: Wiley
12. Monroe CW, Wheeler DR, Newman J. 2015. Nonequilibrium linear response theory: application to Onsager–Stefan–Maxwell diffusion. *Ind. Eng. Chem. Res.* 54:4460–67
13. Fornasiero F, Prausnitz JM, Radke CJ. 2005. Multicomponent diffusion in highly asymmetric systems. An extended Maxwell–Stefan model for starkly different-sized, segment-accessible chain molecules. *Macromolecules* 38:1364–70
14. Monroe CW, Delacourt C. 2013. Continuum transport laws for locally non-neutral concentrated electrolytes. *Electrochim. Acta* 114:649–57
15. Bizeray AM, Howey DA, Monroe CW. 2016. Resolving a discrepancy in diffusion potentials, with a case study for Li-ion batteries. *J. Electrochem. Soc.* 163:E223–29
16. Doyle M, Fuller TF, Newman J. 1993. Modeling of galvanostatic charge and discharge of the lithium/polymer/insertion cell. *J. Electrochem. Soc.* 140:1526–33
17. Fuller TF, Doyle M, Newman J. 1994. Simulation and optimization of the dual lithium ion insertion cell. *J. Electrochem. Soc.* 141:1–10
18. Doyle M, Fuller TF, Newman J. 1994. The importance of the lithium ion transference number in lithium/polymer cells. *Electrochim. Acta* 39:2073–81

19. Sulzer V, Chapman SJ, Please CP, Howey DA, Monroe CW. 2019. Faster lead-acid battery simulations from porous-electrode theory: part I. Physical model. *J. Electrochem. Soc.* 166:A2363–71
20. Liu J, Monroe CW. 2014. Solute-volume effects in electrolyte transport. *Electrochim. Acta* 135:447–60
21. Courtney IA, Tse JS, Mao O, Hafner J, Dahn JR. 1998. Ab initio calculation of the lithium-tin voltage profile. *Phys. Rev. B* 58:15583–88
22. Wolverton C, Zunger A. 1998. First-principles prediction of vacancy order-disorder and intercalation battery voltages in Li_xCoO_2. *Phys. Rev. Lett.* 81:606–9
23. Newman M, Barkema G. 1999. *Monte Carlo Methods in Statistical Physics*. New York: Oxford Univ. Press
24. Van der Ven A, Aydinol MK, Ceder G, Kresse G, Hafner J. 1998. First-principles investigation of phase stability in Li_xCoO_2. *Phys. Rev. B* 58:2975–87
25. Zhou F, Kang K, Maxisch T, Ceder G, Morgan D. 2004. The electronic structure and band gap of $LiFePO_4$ and $LiMnPO_4$. *Solid State Commun.* 132:181–86
26. Ménétrier M, Saadoune I, Levasseur S, Delmas C. 1999. The insulator-metal transition upon lithium deintercalation from $LiCoO_2$: electronic properties and ^7Li NMR study. *J. Mater. Chem.* 9:1135–40
27. Zhou F, Maxisch T, Ceder G. 2006. Configurational electronic entropy and the phase diagram of mixed-valence oxides: the case of Li_xFePO_4. *Phys. Rev. Lett.* 97:155704
28. Hänggi P, Talkner P, Borkovec M. 1990. Reaction-rate theory: fifty years after Kramers. *Rev. Mod. Phys.* 62:251–341
29. Van der Ven A, Thomas JC, Xu Q, Swoboda B, Morgan D. 2008. Nondilute diffusion from first principles: Li diffusion in Li_xTiS_2. *Phys. Rev. B* 78:104306
30. Gomer R. 1990. Diffusion of adsorbates on metal surfaces. *Rep. Prog. Phys.* 53:917–1002
31. Morgan D, Van der Ven A, Ceder G. 2004. Li conductivity in Li_xMPO_4 (M = Mn, Fe, Co, Ni) olivine materials. *Electrochem. Solid-State Lett.* 7:A30–32
32. Van der Ven A, Ceder G. 2000. Lithium diffusion in layered Li_xCoO_2. *Electrochem. Solid-State Lett.* 3:301–4
33. Van der Ven A, Ceder G. 2001. Lithium diffusion mechanisms in layered intercalation compounds. *J. Power Sources* 97–98:529–31
34. Jalem R, Yamamoto Y, Shiiba H, Nakayama M, Munakata H, et al. 2013. Concerted migration mechanism in the Li ion dynamics of garnet-type $Li_7La_3Zr_2O_{12}$. *Chem. Mater.* 25:425–30
35. Malik R, Burch D, Bazant M, Ceder G. 2010. Particle size dependence of the ionic diffusivity. *Nano Lett.* 10:4123–27
36. He X, Zhu Y, Mo Y. 2017. Origin of fast ion diffusion in super-ionic conductors. *Nat. Commun.* 8:15893
37. Islam MS, Fisher CAJ. 2014. Lithium and sodium battery cathode materials: computational insights into voltage, diffusion and nanostructural properties. *Chem. Soc. Rev.* 43:185–204
38. Urban A, Seo DH, Ceder G. 2016. Computational understanding of Li-ion batteries. *NPJ Comput. Mater.* 2:16002
39. Van der Ven A, Thomas J, Puchala B, Natarajan A. 2018. First-principles statistical mechanics of multicomponent crystals. *Annu. Rev. Mater. Res.* 48:27–55
40. Li Y, Chueh WC. 2018. Electrochemical and chemical insertion for energy transformation and switching. *Annu. Rev. Mater. Res.* 48:137–65
41. Darling R, Newman J. 1997. Modeling a porous intercalation electrode with two characteristic particle sizes. *J. Electrochem. Soc.* 144:4201–8
42. Qi Y, Hector LG, James C, Kim KJ. 2014. Lithium concentration dependent elastic properties of battery electrode materials from first principles calculations. *J. Electrochem. Soc.* 161:F3010–18
43. Qi Y, Guo H, Hector LG, Timmons A. 2010. Threefold increase in the Young's modulus of graphite negative electrode during lithium intercalation. *J. Electrochem. Soc.* 157:A558–66
44. Beaulieu LY, Eberman KW, Turner RL, Krause LJ, Dahn JR. 2001. Colossal reversible volume changes in lithium alloys. *Electrochem. Solid-State Lett.* 4:A137–40
45. Itou Y, Ukyo Y. 2005. Performance of $LiNiCoO_2$ materials for advanced lithium-ion batteries. *J. Power Sources* 146:39–44
46. Zhao Y, Stein P, Bai Y, Al-Siraj M, Yang Y, Xu BX. 2019. A review on modeling of electro-chemo-mechanics in lithium-ion batteries. *J. Power Sources* 413:259–83

47. Prussin S. 1961. Generation and distribution of dislocations by solute diffusion. *J. Appl. Phys.* 32:1876–81
48. Christensen J, Newman J. 2006. Stress generation and fracture in lithium insertion materials. *J. Solid State Electrochem.* 10:293–319
49. Christensen J. 2010. Modeling diffusion-induced stress in Li-ion cells with porous electrodes. *J. Electrochem. Soc.* 157:A366–80
50. Zhang X, Shyy W, Sastry AM. 2007. Numerical simulation of intercalation-induced stress in Li-ion battery electrode particles. *J. Electrochem. Soc.* 154:A910–16
51. Cheng YT, Verbrugge MW. 2008. The influence of surface mechanics on diffusion induced stresses within spherical nanoparticles. *J. Appl. Phys.* 104:083521
52. Miller RE, Shenoy VB. 2000. Size-dependent elastic properties of nanosized structural elements. *Nanotechnology* 11:139–47
53. Wang J, Duan H, Huang Z, Karihaloo B. 2006. A scaling law for properties of nano-structured materials. *Proc. R. Soc. A* 462:1355–63
54. Wang J, Huang Z, Duan H, Yu S, Feng X, et al. 2011. Surface stress effect in mechanics of nanostructured materials. *Acta Mech. Solida Sin.* 24:52–82
55. Deshpande R, Cheng YT, Verbrugge MW. 2010. Modeling diffusion-induced stress in nanowire electrode structures. *J. Power Sources* 195:5081–88
56. Chan CK, Peng H, Liu G, McIlwrath K, Zhang XF, et al. 2008. High-performance lithium battery anodes using silicon nanowires. *Nat. Nanotechnol.* 3:31–35
57. Deshpande R, Qi Y, Cheng YT. 2010. Effects of concentration-dependent elastic modulus on diffusion-induced stresses for battery applications. *J. Electrochem. Soc.* 157:A967–71
58. Yang B, He YP, Irsa J, Lundgren C, Ratchford J, Zhao YP. 2012. Effects of composition-dependent modulus, finite concentration and boundary constraint on Li-ion diffusion and stresses in a bilayer Cu-coated Si nano-anode. *J. Power Sources* 204:168–76
59. Hsieh AG, Bhadra S, Hertzberg BJ, Gjeltema PJ, Goy A, et al. 2015. Electrochemical-acoustic time of flight: in operando correlation of physical dynamics with battery charge and health. *Energy Environ. Sci.* 8:1569–77
60. Davies G, Knehr KW, Van Tassell B, Hodson T, Biswas S, et al. 2017. State of charge and state of health estimation using electrochemical acoustic time of flight analysis. *J. Electrochem. Soc.* 164:A2746–55
61. Zhang W, Srinivasan S, Ploehn HJ. 1996. Analysis of transient hydrogen uptake by metal alloy particles. *J. Electrochem. Soc.* 143:4039–47
62. Subramanian VR, Ploehn HJ, White RE. 2000. Shrinking core model for the discharge of a metal hydride electrode. *J. Electrochem. Soc.* 147:2868–73
63. Zhang Q, White RE. 2007. Moving boundary model for the discharge of a $LiCoO_2$ electrode. *J. Electrochem. Soc.* 154:A587–96
64. Srinivasan V, Newman J. 2004. Discharge model for the lithium iron-phosphate electrode. *J. Electrochem. Soc.* 151:A1517–29
65. Srinivasan V, Newman J. 2006. Existence of path-dependence in the $LiFePO_4$ electrode. *Electrochem. Solid-State Lett.* 9:A110–14
66. Christensen J, Newman J. 2006. A mathematical model of stress generation and fracture in lithium manganese oxide. *J. Electrochem. Soc.* 153:A1019–30
67. Deshpande R, Cheng YT, Verbrugge MW, Timmons A. 2011. Diffusion induced stresses and strain energy in a phase-transforming spherical electrode particle. *J. Electrochem. Soc.* 158:A718–24
68. Han B, Van der Ven A, Morgan D, Ceder G. 2004. Electrochemical modeling of intercalation processes with phase field models. *Electrochim. Acta* 49:4691–99
69. Weppner W, Huggins RA. 1977. Determination of the kinetic parameters of mixed-conducting electrodes and application to the system Li_3Sb. *J. Electrochem. Soc.* 124:1569–78
70. Wen CJ, Boukamp BA, Huggins RA, Weppner W. 1979. Thermodynamic and mass transport properties of "LiAl." *J. Electrochem. Soc.* 126:2258–66
71. Singh GK, Ceder G, Bazant MZ. 2008. Intercalation dynamics in rechargeable battery materials: general theory and phase-transformation waves in $LiFePO_4$. *Electrochim. Acta* 53:7599–613

72. Bai P, Cogswell DA, Bazant MZ. 2011. Suppression of phase separation in $LiFePO_4$ nanoparticles during battery discharge. *Nano Lett.* 11:4890–96
73. Li Y, El Gabaly F, Ferguson TR, Smith RB, Bartelt NC, et al. 2014. Current-induced transition from particle-by-particle to concurrent intercalation in phase-separating battery electrodes. *Nat. Mater.* 13:1149–56
74. Tang M, Huang HY, Meethong N, Kao YH, Carter WC, Chiang YM. 2009. Model for the particle size, overpotential, and strain dependence of phase transition pathways in storage electrodes: application to nanoscale olivines. *Chem. Mater.* 21:1557–71
75. Meethong N, Kao YH, Tang M, Huang HY, Carter WC, Chiang YM. 2008. Electrochemically induced phase transformation in nanoscale olivines $Li_{1-x}MPO_4$ (M = Fe, Mn). *Chem. Mater.* 20:6189–98
76. Meethong N, Huang HYS, Carter WC, Chiang YM. 2007. Size-dependent lithium miscibility gap in nanoscale $Li_{1-x}FePO_4$. *Electrochem. Solid-State Lett.* 10:A134–38
77. Wagemaker M, Singh DP, Borghols WJ, Lafont U, Haverkate L, et al. 2011. Dynamic solubility limits in nanosized olivine $LiFePO_4$. *J. Am. Chem. Soc.* 133:10222–28
78. Zhang T, Kamlah M. 2019. Phase-field modeling of the particle size and average concentration dependent miscibility gap in nanoparticles of $Li_xMn_2O_4$, Li_xFePO_4, and Na_xFePO_4 during insertion. *Electrochim. Acta* 298:31–42
79. Newman J, Chapman TW. 1973. Restricted diffusion in binary solutions. *AIChE J.* 19:343–48
80. Kim SU, Monroe CW. 2013. Increasing the rate capability of batteries with electrolyte flow. *Appl. Energy* 103:207–11
81. Lu Y, Tikekar M, Mohanty R, Hendrickson K, Ma L, Archer LA. 2015. Stable cycling of lithium metal batteries using high transference number electrolytes. *Adv. Energy Mater.* 5:1402073
82. Diederichsen KM, McShane EJ, McCloskey BD. 2017. Promising routes to a high Li^+ transference number electrolyte for lithium ion batteries. *ACS Energy Lett.* 2:2563–75
83. Yariv E, Almog Y. 2010. Ionic currents in the presence of supporting electrolytes. *Phys. Rev. Lett.* 105:176101
84. Monroe CW. 2017. Does oxygen transport affect the cell voltages of metal/air batteries? *J. Electrochem. Soc* 164:E3547–51
85. Gebbie MA, Dobbs HA, Valtiner M, Israelachvili JN. 2015. Long-range electrostatic screening in ionic liquids. *PNAS* 112:7432–37
86. Lee AA, Vella D, Perkin S, Goriely A. 2015. Are room-temperature ionic liquids dilute electrolytes? *J. Phys. Chem. Lett.* 6:159–63
87. Richardson G, Foster JM, Sethurajan AK, Krachkovskiy SA, Halalay IC, et al. 2018. The effect of ionic aggregates on the transport of charged species in lithium electrolyte solutions. *J. Electrochem. Soc.* 165:H561–67
88. Clark S, Latz A, Horstmann B. 2017. Rational development of neutral aqueous electrolytes for zinc-air batteries. *ChemSusChem* 10:4735–47
89. Grossfield A, Ren P, Ponder JW. 2003. Ion solvation thermodynamics from simulation with a polarizable force field. *J. Am. Chem. Soc.* 125:15671–82
90. Li Z, Smith GD, Bedrov D. 2012. Li^+ solvation and transport properties in ionic liquid/lithium salt mixtures: a molecular dynamics simulation study. *J. Phys. Chem. B* 116:12801–9
91. Abe T, Fukuda H, Iriyama Y, Ogumi Z. 2004. Solvated Li-ion transfer at interface between graphite and electrolyte. *J. Electrochem. Soc.* 151:A1120–23
92. Landstorfer M, Guhlke C, Dreyer W. 2016. Theory and structure of the metal-electrolyte interface incorporating adsorption and solvation effects. *Electrochim. Acta* 201:187–219
93. Suo L, Hu YS, Li H, Armand M, Chen L. 2013. A new class of solvent-in-salt electrolyte for high-energy rechargeable metallic lithium batteries. *Nat. Commun.* 4:1481
94. McEldrew M, Goodwin ZAH, Kornyshev AA, Bazant MZ. 2018. Theory of the double layer in water-in-salt electrolytes. *J. Phys. Chem. Lett.* 9:5840–46
95. Xu K. 2014. Electrolytes and interphases in Li-ion batteries and beyond. *Chem. Rev.* 114:11503–618
96. Wyllie MRJ, Rose WD. 1950. Some theoretical considerations related to the quantitative evaluation of the physical characteristics of reservoir rock from electrical log data. *J. Pet. Technol.* 2:105–18

97. Zalc JM, Reyes SC, Iglesia E. 2004. The effects of diffusion mechanism and void structure on transport rates and tortuosity factors in complex porous structures. *Chem. Eng. Sci.* 59:2947–60
98. Wiedenmann D, Keller L, Holzer L, Stojadinović J, Münch B, et al. 2013. Three-dimensional pore structure and ion conductivity of porous ceramic diaphragms. *AIChE J.* 59:1446–57
99. Landesfeind J, Hattendorff J, Ehrl A, Wall WA, Gasteiger HA. 2016. Tortuosity determination of battery electrodes and separators by impedance spectroscopy. *J. Electrochem. Soc.* 163:A1373–87
100. Torquato S. 2013. *Random Heterogeneous Materials: Microstructure and Macroscopic Properties*. New York: Springer
101. Stauffer D, Aharony A. 1994. *Introduction to Percolation Theory*. Philadelphia: Taylor & Francis. 2nd ed.
102. Bruggeman DAG. 1935. Berechnung verschiedener physikalischer Konstanten von heterogenen Substanzen. I. Dielektrizitätskonstanten und Leitfähigkeiten der Mischkörper aus isotropen Substanzen. *Ann. Phys.* 416:636–64
103. Tjaden B, Cooper SJ, Brett DJ, Kramer D, Shearing PR. 2016. On the origin and application of the Bruggeman correlation for analysing transport phenomena in electrochemical systems. *Curr. Opin. Chem. Eng.* 12:44–51
104. Ferguson TR, Bazant MZ. 2012. Nonequilibrium thermodynamics of porous electrodes. *J. Electrochem. Soc.* 159:A1967–85
105. Ender M, Joos J, Carraro T, Ivers-Tiffe E. 2011. Three-dimensional reconstruction of a composite cathode for lithium-ion cells. *Electrochem. Commun.* 13:166–68
106. Ebner M, Wood V. 2015. Tool for tortuosity estimation in lithium ion battery porous electrodes. *J. Electrochem. Soc.* 162:A3064–70
107. Cooper S, Eastwood D, Gelb J, Damblanc G, Brett D, et al. 2014. Image based modelling of microstructural heterogeneity in $LiFePO_4$ electrodes for Li-ion batteries. *J. Power Sources* 247:1033–39
108. Liu J, Rahimian SK, Monroe CW. 2016. Capacity-limiting mechanisms in Li/O_2 batteries. *Phys. Chem. Chem. Phys.* 18:22840–51
109. Mullins WW, Sekerka RF. 1963. Morphological stability of a particle growing by diffusion or heat flow. *J. Appl. Phys.* 34:323–29
110. Mullins WW, Sekerka RF. 1964. Stability of a planar interface during solidification of a dilute binary alloy. *J. Appl. Phys.* 35:444–51
111. Aogaki R, Makino T. 1981. Theory of powdered metal formation in electrochemistry—morphological instability in galvanostatic crystal growth under diffusion control. *Electrochim. Acta* 26:1509–17
112. Aogaki R. 1982. Image analysis of morphological instability in galvanostatic electrocrystallization: I . General expression for the growth mode of surface irregularities. *J. Electrochem. Soc.* 129:2442–46
113. Sundström LG, Bark FH. 1995. On morphological instability during electrodeposition with a stagnant binary electrolyte. *Electrochim. Acta* 40:599–614
114. Monroe C, Newman J. 2004. The effect of interfacial deformation on electrodeposition kinetics. *J. Electrochem. Soc.* 151:A880–86
115. Monroe C, Newman J. 2005. The impact of elastic deformation on deposition kinetics at lithium/polymer interfaces. *J. Electrochem. Soc.* 152:A396–404
116. Despić A, Popov KI. 1972. Transport-controlled deposition and dissolution of metals. In *Modern Aspects of Electrochemistry No. 7*, ed. BE Conway, JO Bockris, pp. 199–313. Boston: Springer
117. Witten TA, Sander LM. 1981. Diffusion-limited aggregation, a kinetic critical phenomenon. *Phys. Rev. Lett.* 47:1400–3
118. Chazalviel JN. 1990. Electrochemical aspects of the generation of ramified metallic electrodeposits. *Phys. Rev. A* 42:7355–67
119. Barton JL, Bockris JO. 1962. The electrolytic growth of dendrites from ionic solutions. *Proc. R. Soc. A* 268:485–505
120. Diggle JW, Despic AR, Bockris JO. 1969. The mechanism of the dendritic electrocrystallization of zinc. *J. Electrochem. Soc.* 116:1503–14
121. Dollé M, Sannier L, Beaudoin B, Trentin M, Tarascon JM. 2002. Live scanning electron microscope observations of dendritic growth in lithium/polymer cells. *Electrochem. Solid-State Lett.* 5:A286–89
122. Monroe C, Newman J. 2003. Dendrite growth in lithium/polymer systems: a propagation model for liquid electrolytes under galvanostatic conditions. *J. Electrochem. Soc.* 150:A1377–84

123. Han F, Westover AS, Yue J, Fan X, Wang F, et al. 2019. High electronic conductivity as the origin of lithium dendrite formation within solid electrolytes. *Nat. Energy* 4:187–96
124. Zhu Y, He X, Mo Y. 2016. First principles study on electrochemical and chemical stability of solid electrolyte–electrode interfaces in all-solid-state Li-ion batteries. *J. Mater. Chem. A* 4:3253–66
125. Zhang Z, Shao Y, Lotsch B, Hu YS, Li H, et al. 2018. New horizons for inorganic solid state ion conductors. *Energy Environ. Sci.* 11:1945–76
126. Kornyshev A, Vorotyntsev M. 1981. Conductivity and space charge phenomena in solid electrolytes with one mobile charge carrier species, a review with original material. *Electrochim. Acta* 26:303–23
127. Yamamoto K, Iriyama Y, Asaka T, Hirayama T, Fujita H, et al. 2010. Dynamic visualization of the electric potential in an all-solid-state rechargeable lithium battery. *Angew. Chem.* 49:4414–17
128. Braun S, Yada C, Latz A. 2015. Thermodynamically consistent model for space-charge-layer formation in a solid electrolyte. *J. Phys. Chem. C* 119:22281–88
129. Li G, Monroe CW. 2019. Dendrite nucleation in lithium-conductive ceramics. *Phys. Chem. Chem. Phys.* 21:20354–59
130. De Jonghe LC, Feldman L, Beuchele A. 1981. Slow degradation and electron conduction in sodium/beta-aluminas. *J. Mater. Sci.* 16:780–86
131. De Jonghe LC. 1982. Transport number gradients and solid electrolyte degradation. *J. Electrochem. Soc.* 129:752–55
132. Feldman LA, De Jonghe LC. 1982. Initiation of mode I degradation in sodium-beta alumina electrolytes. *J. Mater. Sci.* 17:517–24
133. Porz L, Swamy T, Sheldon BW, Rettenwander D, Frömling T, et al. 2017. Mechanism of lithium metal penetration through inorganic solid electrolytes. *Adv. Energy Mater.* 7:1701003
134. Ahmad Z, Viswanathan V. 2017. Stability of electrodeposition at solid-solid interfaces and implications for metal anodes. *Phys. Rev. Lett.* 119:056003
135. Kasemchainan J, Zekoll S, Spencer Jolly D, Ning Z, Hartley GO, et al. 2019. Critical stripping current leads to dendrite formation on plating in lithium anode solid electrolyte cells. *Nat. Mater.* 18:1105–11
136. Krauskopf T, Hartmann H, Zeier WG, Janek J. 2019. Toward a fundamental understanding of the lithium metal anode in solid-state batteries—an electrochemo-mechanical study on the garnet-type solid electrolyte $Li_{6.25}Al_{0.25}La_3Zr_2O_{12}$. *ACS Appl. Mater. Interfaces* 11:14463–77
137. Wang MJ, Choudhury R, Sakamoto J. 2019. Characterizing the Li-solid-electrolyte interface dynamics as a function of stack pressure and current density. *Joule* 3:2165–78
138. Masias A, Felten N, Garcia-Mendez R, Wolfenstine J, Sakamoto J. 2019. Elastic, plastic, and creep mechanical properties of lithium metal. *J. Mater. Sci.* 54:2585–600
139. Sharafi A, Meyer HM, Nanda J, Wolfenstine J, Sakamoto J. 2016. Characterizing the $Li_7La_3Zr_2O_{12}$ interface stability and kinetics as a function of temperature and current density. *J. Power Sources* 302:135–39
140. Sharafi A, Kazyak E, Davis AL, Yu S, Thompson T, et al. 2017. Surface chemistry mechanism of ultra-low interfacial resistance in the solid-state electrolyte $Li_7La_3Zr_2O_{12}$. *Chem. Mater.* 29:7961–68
141. Fu KK, Gong Y, Liu B, Zhu Y, Xu S, et al. 2017. Toward garnet electrolyte–based Li metal batteries: an ultrathin, highly effective, artificial solid-state electrolyte/metallic Li interface. *Sci. Adv.* 3:e1601659
142. Cheng EJ, Sharafi A, Sakamoto J. 2017. Intergranular Li metal propagation through polycrystalline $Li_{6.25}Al_{0.25}La_3Zr_2O_{12}$ ceramic electrolyte. *Electrochim. Acta* 223:85–91
143. Cheng L, Chen W, Kunz M, Persson K, Tamura N, et al. 2015. Effect of surface microstructure on electrochemical performance of garnet solid electrolytes. *ACS Appl. Mater. Interfaces* 7:2073–81
144. Sharafi A, Haslam CG, Kerns RD, Wolfenstine J, Sakamoto J. 2017. Controlling and correlating the effect of grain size with the mechanical and electrochemical properties of $Li_7La_3Zr_2O_{12}$ solid-state electrolyte. *J. Mater. Chem. A* 5:21491–504
145. Yu S, Siegel DJ. 2017. Grain boundary contributions to Li-ion transport in the solid electrolyte $Li_7La_3Zr_2O_{12}$ (LLZO). *Chem. Mater.* 29:9639–47
146. Ma C, Chen K, Liang C, Nan CW, Ishikawa R, et al. 2014. Atomic-scale origin of the large grain-boundary resistance in perovskite Li-ion-conducting solid electrolytes. *Energy Environ. Sci.* 7:1638–42

147. Bucci G, Swamy T, Chiang YM, Carter WC. 2017. Modeling of internal mechanical failure of all-solid-state batteries during electrochemical cycling, and implications for battery design. *J. Mater. Chem. A* 5:19422–30
148. Bucci G, Talamini B, Balakrishna AR, Chiang YM, Carter WC. 2018. Mechanical instability of electrode-electrolyte interfaces in solid-state batteries. *Phys. Rev. Mater.* 2:105407
149. Van der Ven A, Ceder G, Asta M, Tepesch PD. 2001. First-principles theory of ionic diffusion with nondilute carriers. *Phys. Rev. B* 64:184307
150. Van der Ven A, Bhattacharya J, Belak AA. 2013. Understanding Li diffusion in Li-intercalation compounds. *Acc. Chem. Res.* 46:1216–25
151. Shetty DK, Virkar AV, Gordon RS. 1978. Electrolytic degradation of lithia-stabilized polycrystalline β''-alumina. In *Fracture Mechanics of Ceramics*, Vol. 4: *Crack Growth and Microstructure*, ed. RC Bradt, DPH Hasselman, FF Lange, pp. 651–65. New York: Plenum